1.0

1.1

1.25   1.4   1.6

2.8   2.5

3.0   2.2

2.0

1.8

MICROCOPY RESOLUTION TEST CHART

ADA111838

AFGL-TR-81-0205

CLOUD TRACKING FROM SATELLITE PICTURES

Uwe L. Haass

Colorado State University
Electrical Engineering and Atmospheric
Science Departments
Ft Collins, Colorado 80523

July 1981

Scientific Report No. 2

Approved for public release; distribution unlimited

AIR FORCE GEOPHYSICS LABORATORY
AIR FORCE SYSTEMS COMMAND
UNITED STATES AIR FORCE
HANSCOM AFB, MASSACHUSETTS 01731

DTIC
ELECTE
MAR 9 1982
S
B

DTIC FILE COPY

82 03 09 052

REPORT DOCUMENTATION PAGE		READ INSTRUCTIONS BEFORE COMPLETING FORM
1. REPORT NUMBER AFGL-TR-81-0205	2. GOVT ACCESSION NO. AD-A111 838	3. RECIPIENT'S CATALOG NUMBER
4. TITLE (and Subtitle) Cloud Tracking from Satellite Pictures		5. TYPE OF REPORT & PERIOD COVERED Scientific Report No. 2
		6. PERFORMING ORG. REPORT NUMBER
7. AUTHOR(s) Uwe L. Haass		8. CONTRACT OR GRANT NUMBER(s) F19628-78-C-0207
9. PERFORMING ORGANIZATION NAME AND ADDRESS Colorado State University Electrical Engineering and Atmospheric Science Departments Ft. Collins, Colorado 80523		10. PROGRAM ELEMENT, PROJECT, TASK AREA & WORK UNIT NUMBERS 62101F 667008AA
11. CONTROLLING OFFICE NAME AND ADDRESS Air Force Geophysics Laboratory Hanscom AFB, Massachusetts 01731 Monitor/H. Stuart Muench/LYP		12. REPORT DATE July 1981
		13. NUMBER OF PAGES 148
14. MONITORING AGENCY NAME & ADDRESS(if different from Controlling Office)		15. SECURITY CLASS. (of this report) Unclassified
		15a. DECLASSIFICATION/DOWNGRADING SCHEDULE

16. DISTRIBUTION STATEMENT (of this Report)

    Approved for public release; distribution unlimited

17. DISTRIBUTION STATEMENT (of the abstract entered in Block 20, if different from Report)

18. SUPPLEMENTARY NOTES
In partial fulfillment of the requirements for the Degree of Doctor of
Philosophy, Colorado State University, Ft. Collins, CO

19. KEY WORDS (Continue on reverse side if necessary and identify by block number)
Satellite Pictures
Lateral Cloud displacement
cloud tracking
cloud motion forecasting
cloud rotation

20. ABSTRACT (Continue on reverse side if necessary and identify by block number)
Satellite pictures taken in short time intervals are employed to estimate
the lateral (x-y) and rotational displacement of clouds. Several methods of
motion analysis are introduced based on different signal characterizations and
various degrees of image abstraction. Using the discrete luminance information
(half-tone picture), the maximum of the inner product surface of two consecutive
images serves as a lateral displacement estimator. This dissertation demonstrates
how the maximum peak detectability can be improved by prefiltering with a non
causal planar least-squares inverse filter. Although this filter is derived

from theoretical considerations, the resulting high-pass frequency characteris-tics commends its use for another reason: since most of the cloud information, such as edges and texture, is embedded in the high-frequency parts of the image, the subsequent inner product operation takes only the homogeneous displacement of these features into account. For clouds that have undergone severe shape changes, a gradual shift to less restrictive frequency characteristics is suggested.

If the luminance values are fit to a bivariate normal surface, clouds or cloud fields can be traced by following the ellipses of equal density. This method retrieves lateral displacement, rotation and size changes.

Another technique makes use of a closed contour of the cloud, either the boundary or any contour of constant gray-level. This contour is traced, re-sampled and transformed into a Fourier descriptor (FD) series. The resulting coefficients reveal direct information about lateral displacement, rotation and scale change. For sufficiently smooth contours, this information can be obtained from very few low-order coefficients. The inverse transform of the two lowest-order coefficients is an ellipse approximating the original contour in the least-squares sense.

Finally, the problem of parameter modelling and forecasting is approached by the introduction of a Kalman filter. Linear and non-linear models are discussed. The analysis of several cloud motion case studies, however, revealed a multitude of severely non-stationary effects that could not be accounted for. Further research is recommended.

ABSTRACT

CLOUD TRACKING FROM SATELLITE PICTURES

Satellite pictures taken in short time intervals are employed to estimate the lateral (x-y) and rotational displacement of clouds. Several methods of motion analysis are introduced based on different signal characterizations and various degrees of image abstraction. Using the discrete luminance information (half-tone picture), the maximum of the inner product surface of two consecutive images serves as a lateral displacement estimator. This dissertation demonstrates how the maximum peak detectability can be improved by prefiltering with a non-causal planar least-squares inverse filter. Although this filter is derived from theoretical considerations, the resulting high-pass frequency characteristic commends its use for another reason: since most of the cloud information, such as edges and texture, is embedded in the high-frequency parts of the image, the subsequent inner product operation takes only the homogeneous displacement of these features into account. For clouds that have undergone severe shape changes, a gradual shift to less restrictive frequency characteristics is suggested.

If the luminance values are fit to a vivariate normal surface, clouds or cloud fields can be traced by following the ellipses of equal density. This method retrieves lateral displacement, rotation and size changes.

Another technique makes use of a closed contour of the cloud, either the boundary or any contour of constant gray-level. This contour

is traced, re-sampled and transformed into a Fourier descriptor (FD) series. The resulting coefficients reveal direct information about lateral displacement, rotation and scale change. For sufficiently smooth contours, this information can be obtained from very few low-order coefficients. The inverse transform of the two lowest-order coefficients is an ellipse approximating the original contour in the least-squares sense.

Finally, the problem of parameter modelling and forecasting is approached by the introduction of a Kalman filter. Linear and non-linear models are discussed. The analysis of several cloud motion case studies, however, revealed a multitude of severely non-stationary effects that could not be accounted for. Further research is recommended.

Uwe L. Haass
Electrical Engineering Department
Colorado State University
Fort Collins, Colorado 80523
Spring, 1981

ACKNOWLEDGEMENTS

I wish to acknowledge the assistance and friendship of my
adviser, Thomas A. Brubaker. I also thank Dr. T. Vonder Haar, Dr.
G.K. Lee and Dr. C.W. Wilmsen for serving on my graduate committee.
The completion of this work would not have been possible without the
stimulating interaction and professional advice from other faculty
and graduate students of the Departments of Electrical Engineering and
Atmospheric Science at Colorado State University, notably Dr. Louis L.
Scharf, Dr. Eric A. Smith, Dr. Aloysius A. Beex, Jean-Pierre Dugré,
and Norman Buss.

Special appreciation goes to my colleagues of the Digital Systems
Laboratory for their moral support.

TABLE OF CONTENTS

LIST OF TABLES

LIST OF FIGURES

CHAPTER 1

INTRODUCTION

With the advent of high-resolution imaging techniques, it has
become feasible to employ pictures taken from geostationary satellites
for the interpretation and prediction of atmospheric processes in the
mesoscale range. Although polar-orbiting satellites with a sun-
synchronous orbit have a relatively low flight altitude of less than
1000 km and thus provide images with high resolution, areas in the mid-
latitudes are over-flown only twice a day. Geostationary meteorological
satellites, however, like the American GOES or the European Meteosat,
orbit in 36,000 km, but transmit a discretized, digital image of the
full earth disc each half an hour, with subpoint resolution of 1 - 2.5
km in the visible channel and 5 - 8 km in the thermal infrared (i.e.,
approximately 11 μm) channel. For smaller areas of coverage, higher
repetition rates can be selected by ground control. High reception
rates of up to every 3 minutes allow the meteorological image analyst
to detect fast changing features that bear relevance in local forecast-
ing, but might be negligible for the description of synoptic-scale
situations.

In spite of the introduction of satellite-based radiometers for
other spectral bands, such as the water vapor channel around 6 μm on
Meteosat, or microwave sounding devices aboard the spacecrafts, the
classic meteorological analysis from satellites is based on the inter-
pretation of cloud images. Clouds are the most regularly visible

1

phenomenon providing excellent information on fundamental conditions. The monitoring of cloud clusters, vorticity centers, frontal bands as well as single clouds are of great importance to the local forecaster. One of the foremost objectives is the identification and prediction of severe storms. For a detailed forecast, however, it is essential to obtain the cloud parameters not only qualitatively but also quantitatively.

With the support of computerized digital image processing facilities the parameters of interest are retrieved and displayed such that most of the information is processed, formatted and then made available to the analyst who operates as a 'man-in-the-loop.' Most of the conclusions are based on the motion of clouds and their respective top temperature. Motion and size parameters of a cloud can be employed to estimate wind fields [1,2] as well as to establish models of cloud development and extrapolate from past observations.

Current cloud displacement estimators comprise the subjective film loop technique [3], the 'correlation' technique [4,5] and the ISODATA method [6,7], an intricate cluster analysis technique. The objective of this research is to develop estimators that reveal not only information on lateral (x-y) cloud displacement, but also on rotation and size changes. The latter two subjects are new in the quantitative cloud analysis. Several methods will be introduced in this work, based on different signal characterizations and various degrees of image abstraction.

In Chapter 2 various approaches to the signal representation of cloud images are discussed. The classical method of estimating lateral displacement employs the luminance (gray-tone) information of

the discretized digital image. The estimate is obtained by identifying the location of the maximum of the inner-product surface (for energy signals) or of the spatial cross-correlation (for power signals) of two consecutive pictures. Improvement of the maximum-peak detectability by means of prefiltering is discussed in Chapter 3. In Chapter 4 it is shown how the luminance values of a cloud or a cloud field can be fitted to a bivariate Gaussian function. The lines of constant density are ellipses about the center of luminance gravity. By following these ellipses through a sequence of images, clouds may be traced and information obtained on rotation, displacement and size changes. Chapter 5 deals with the analysis of cloud contours. A contour is traced with constant velocity. In equidistant time intervals, the values x and y of the contour points are combined to a complex number $z = x + jy$. This complex series can be transformed into a Discrete Fourier Series (Fourier descriptor). The resulting coefficients reveal direct information on lateral and rotational displacement as well as the scale change of the contour. A numeric matching algorithm determines the amount of rotation, shifting and scale change in order to match two contours in the optimum sense. Matching can be performed even on the basis of a truncated Fourier descriptor series, thus reducing the computational requirements.

The inverse transformation of a descriptor series truncated to the three lowest coefficients is an ellipse approximating the original contour in the least-squares sense. These ellipses can be tracked and, if desired, be compared with the ellipses obtained from the bivariate Gaussian luminance fit.

The problem of parameter forecasting is approached in Chapter 6. A Kalman filter is introduced to track cloud parameters and obtain one-step predicted values, such as the geometric parameters of an ellipse from a given series of elliptic approximations. Linear and non-linear models and the respective requirements for a-priori information are discussed. The work concludes with a simple case study.

CHAPTER 2

SIGNAL ANALYSIS

2.1 The Inner Product

A digital satellite image with clouds is given on a Cartesian matrix grid at times $t = t_i$, $i = 0, 1, 2, \ldots$ by the image sequence

$$\{x_i(n,m)\}, \quad n = 0, \ldots N - 1; m = 0, 1 \ldots M - 1, \qquad (1)$$

with x representing the non-negative digitized brightness value, e.g., an integer number between 0 (= black) and 255 (= white, for 8-bit representation). For displacement analysis, all images have to be navigated to some reference mark, and, if possible, the brightness of the clouds adjusted for sun angle changes.

The image (1) is a combined time-space process and can be considered as deterministic in time and space, deterministic in space but random in time (or vice-versa), or random in both space and time. Although atmospheric processes seem to be described most appropriately by random variables and stochastic processes, a statistical space characterization of the cloud image (1) is problematic. The customary approach of defining an image as a realization of a two-dimensional Gaussian random field is often too simplistic and cannot account for the existence of well defined edges, contours and texture [8]. Additional problems arise with the background. It cannot be considered as additive noise since it is partially occluded by the clouds. This implies that a complete statistical description of the time-space

5

process (1) cannot be easily obtained. Rather than regarding each single pixel (i.e., picture element) of (1) as belonging to the domain of the process realization, the following view has been adopted. Each single image is a noisy measurement of time-varying parameters such as location, size and cloud top temperature. Instead of estimating the statistics of each pixel, the goal is to (i) extract the parameters of interest from each image and (ii) develop predictors for these parameters on the basis of past measurements.

The author is convinced that models based on structural parameters are closer to the aim of the analysis of the underlying meteorological processes and therefore preferred to the classical decomposition of the signal into orthogonal functions.

With the exception of snow-covered terrain and occasional sea-surface reflection, the background of satellite images is usually darker than the clouds. To remove disturbing influences on displacement analysis, the background is set to zero (= black) by either subtraction or clipping at a threshold level. Snow-covered ground is identified by comparison with the reflected radiance in the infrared (IR) bands [9]. Furthermore let us assume that the cloud of interest is completely defined within the image frame. Since the cloud image sequence $\{x(n,m)\}$ then is zero outside some area of support $0 \leq n \leq N-1$, $0 \leq m \leq M-1$, it belongs to the class of finite area sequences [10]. Finite area sequences are energy signals, i.e.,

$$0 \leq \| x(n,m) \|^2 < \infty \tag{2}$$

with the energy of $x(n,m)$ defined as

$$\| x(n,m) \|^2 = \langle x(n,m), x(n,m) \rangle = \sum_{n=0}^{N=1} \sum_{m=0}^{M=1} x^2(n,m) \tag{3}$$

The operation $\| \ldots \|^2$ also is called the norm, and $<\ldots>$ denotes the inner product. These signals describe the ℓ_2 space. The inner product of two sequences $\{x(n,m)\}$ and $\{y(n,m)\}$ with both areas of support given as $0 \leq n \leq N-1$, $0 \leq m \leq M-1$, is defined as

$$K_{xy}(0,0) = <x(n,m), y(n,m)>$$

$$= \sum_{m=0}^{M-1} \sum_{n=0}^{N-1} x(n,m) \, y(n,m). \tag{4}$$

If the sequence $\{y(n,m)\}$ is displaced by ν and μ, we obtain

$$K_{xy}(\nu,\mu) = \sum_{m=0}^{M-1} \sum_{n=0}^{N-1} x(n,m) \, y(n-\nu,m-\mu). \tag{5}$$

If ν,μ in (5) are varied from $0 \ldots N-1$, $0 \ldots M-1$, there is at least one set of indices $\hat{\nu}$ and $\hat{\mu}$ such that K_{xy} is maximum. For the case that $\{y(n,m)\}$ is a shifted replica of $\{x(n,m)\}$, i.e.,

$$\{y(n,m)\} = \{x(n-m_0,m-m_0)\},$$

the absolute maximum of $K_{xy}(.)$ is obtained for $\hat{\nu} = n_0$, $\hat{\mu} = m_0$. Hence the inner product $K_{xy}(.)$ can be used to identify the same cloud in two consecutive images and estimate its lateral displacement.

Although $K_{xy}(.)$ is commonly placed among cross-correlation estimators, the inner product is not based on any probabilistic descriptions. The cross-correlation of a random field is defined as a statistical expected value type of operation involving the joint probability density function [11]. However a random field of energy signals is dynamic enough that statistical inferences may not be made by the analysis of a single image. Displacement estimation with the inner product (5) is a classical operation in image processing [12-14]. In spite of the absence of any statistical assumptions it is commonly called the "cross-correlation" method.

Sometimes the displacement of features is to be estimated within scenes that cannot be described as energy signals but as a space-truncated power signal. Assume that the feature image $\{x(n,m)\}$ of size L, K is to be matched within a large search image $\{y(n,m)\}$ of size N, M. In those instances a maximum of the inner product (5) would not necessarily indicate optimum fit. Hence the normalized 'correlation-coefficient' surface [4, ., 12-15] is introduced as

$$k_{xy}(\nu,\mu) = \frac{\sum\limits_{l=0}^{L-1} \sum\limits_{k=0}^{K-1} x(l,k)\, y(l-\nu,\, k-\mu)}{\left[\sum\limits_{l=0}^{L-1} \sum\limits_{k=0}^{K-1} x^2(l,k)\right]^{\frac{1}{2}} \left[\sum\limits_{l=0}^{L-1} \sum\limits_{k=0}^{K-1} y^2(l-\nu,k-\mu)\right]^{\frac{1}{2}}} \qquad (6)$$

The performance of this operator depends on the size of the feature image and the local statistics of both feature and search area [16]. If the sequences $\{x(n,m)\}$ and $\{y(n,m)\}$ are finite area sequences with identical extensions, the denominator of (6) is a constant, and the numerator is equal to the inner product (5).

Since the background removal is often desired, the influence of this operation on the inner product needs careful consideration. Background removal by clipping is performed according to

$$x_c(n,m) = \begin{cases} x(n,m) & \text{for } x(n,m) \leq c \\ 0 & \text{otherwise} \end{cases} \qquad (7)$$

with c a specified threshold. Background is subtracted by

$$x_s(n,m) = \begin{cases} x(n,m) - c & \text{for } x(n,m) \leq c \\ 0 & \text{otherwise} \end{cases} \qquad (8)$$

Since

$$x_c(n,m) = x_s(n,m) + c,$$

the inner products of $\{x_c(n,m)\}$ and $\{x_s(n,m)\}$ are related as

$$\langle x_c(n,m), x_c(n,m)\rangle = \langle x_s(n,m), x_s(n,m)\rangle$$
$$+ \langle c \cdot q(x_s(n,m)), c \cdot q(x_s(n,m))\rangle \qquad (9)$$

with the plateau function

$$q(x_s(n,m)) = \begin{cases} 1 & \text{for } x_s(.) > 0 \\ 0 & \text{otherwise .} \end{cases} \qquad (10)$$

Equation (9) implies that the inner product of the clipped signal is equal to the inner product of the subtracted signal plus the inner product of the plateau function $c \cdot q(.)$ and hence introduces a bias term depending on the threshold level. Therefore the subtraction method with subsequent dynamic range widening is preferred.

In spite of the author's perseverance in the distinction of inner product and cross-correlation, a particular random model can be assumed for finite area sequences that establishes identity of both operations. With the finite area sequence $\{x(n,m)\}$ being zero outside the rectangle $0 \leq n \leq N-1$, $0 \leq m \leq M-1$, the following random process is constructed:

$$X(n,m) = X(n-V, m-W) \qquad (11)$$

with V, W two independent random variables of uniform distribution, i.e., $V = U[0, Z_n]$ and $W = U[0, Z_m]$. The parameters Z_n and Z_m define the limits of the random displacement of the sequence $\{x(n,m)\}$. The statistical cross-correlation of this process is given by

$$E\{X_1(n,m)\, X_2(n,m)\}$$
$$= E\{E\{X_1(n,m)\, X_2(n,m)|V_1=v_1, V_2=v_2, W_1=w_1, W_2=w_2\}\}. \qquad (12)$$

With $v_2 - v_1 = \xi$, $w_2 - w_1 = \eta$, i.e.,

$$x_2(n,m) - x_1(n-\xi, m-\eta),$$

the interior expected value of (12) becomes

$$\sum_{n=0}^{N} \sum_{m=0}^{M} x_1(n,m) \; x_1(n-\xi, \; m-\eta))/ \sum_{n=0}^{Z_n+N} \sum_{m=0}^{Z_m+M} q(x_1(n,m) \cdot x_1(n-\xi, m-\eta)),$$

$$(13)$$

with the q-function as defined in (10).

The expected value of this expression then is, for the given probability distribution, the cross-correlation

$$E\{X(n,m) \; X(n-\xi, m-\eta)\}$$

$$= \frac{1}{(Z_n+N)(Z_m+M)} \sum_{n=0}^{N} \sum_{m=0}^{M} x(n,m) \; x(n-\xi, m-\eta). \qquad (14)$$

This result is identical to the inner product (5) times a constant factor. Remember that this relationship holds only for the random displacement with uniform distribution. Since the motion of clouds as well as many other physical objects is not governed by a uniform displacement probability but rather by dynamic equations, the short-comings of the inner product as correlation estimator are apparent.

2.2 Spectrum and Moments

For finite area sequences, the two-dimensional discrete Fourier transform (DFT) is defined as [10, p. 117]

$$X(p,q) = DFT \{x(n,m)\}$$

$$= \sum_{n=0}^{N-1} \sum_{m=0}^{M-1} x(n,m) \; \exp \{-2\pi j(\frac{pn}{N} + \frac{qm}{M})\} \qquad (15)$$

where $j = \sqrt{-1}$, and the variables p,q are the spatial frequency wave numbers. The numbers $X(p,q)$ are the Fourier series coefficients of a periodic extension of $\{x(n,m)\}$. From the definition (15) it follows that the two-dimensional DFT is a separable transform, i.e., it can be implemented as a sequence of one-dimensional DFT's. The sequence

{X(p,q)} is also referred to as the Fourier spectrum, or briefly, spectrum of {x(n,m)}. It can be written as

$$X(p,q) = A_x(p,q) \ \exp \{-j\phi_x(p,q)\} \qquad (16)$$

with $A_x(.)$ the amplitude and $\phi_x(p,q) = \arg [X(p,q)]$ its phase. Alternatively, X(p,q) can be expressed as

$$X(p,q) = X_R(p,q) + j \ X_I(p,q), \qquad (17)$$

$X_R(.)$ denoting the real part and $X_I(.)$ the imaginary part. Amplitude and phase is commonly replaced by the magnitude

$$|X(p,q)| = (X_R{}^2(p,q) + X_I{}^2(p,q))^{\frac{1}{2}} \qquad (18)$$

and the principle phase

$$ARG \ [X(p,q)] = \tan^{-1} \frac{X_I(p,q)}{X_R(p,q)} \qquad (19)$$

Note however that magnitude and principle phase are ambiguous with respect to amplitude and phase: (i) the magnitude is non-negative by definition and thus introduces phase discontinuities of $\pm\pi$ whenever the amplitude changes its sign; (ii) the inverse tangent function leads to phase discontinuities of $\pm\pi$ or $\pm2\pi$ according to its definition *).

The product of the spectra of two finite area sequences {x(n,m)} and {y(n,m)} is the Fourier transform of the inner product $K_{xy}(\nu,\mu)$. If {y(n,m)} is a replica of {x(n,m)}, but shifted by n_o and m_o, the cross-spectrum becomes

---

*) Most FORTRAN libraries contain two different inverse tangent functions: ATAN(X) and ATAN2(A,B). Our definition of $\tan^{-1}$ coincides with the two-argument function ATAN2(A,B). The difference is illustrated in the following table:

ϕ	0	$\pi/4$	$\pi/2$	$3\pi/4$	π	$5\pi/4$	$3\pi/2$	$7\pi/4$	2π
ATAN2	0	$\pi/4$	$\pi/2$	$3\pi/4$	$-\pi$	$3\pi/4$	$-\pi/2$	$-\pi/4$	0
ATAN	0	$\pi/4$	$-\pi/2$	$-\pi/4$	0	$\pi/4$	$-\pi/2$	$-\pi/4$	0

$$X(p,q)Y^*(p,q) = A^2(p,q) \quad \exp \quad \{-j2\pi(\frac{n_o}{N} + \frac{m_o}{M})\} \tag{20}$$

Hence the displacement estimation could be performed equivalently in the frequency domain by evaluating the phase of the cross-spectrum. For reasons stated above, the principle phase is wrapped around multiple values of π and therefore does not permit immediate visualization of the phase behavior. The evaluation of the continuous phase, also called phase unwrapping, has gained considerable interest in the numerical evaluation of the cepstrum [10, p. 508; 17, 18]. The cepstrum is defined as the inverse Fourier transform of the complex logarithm of the spectrum. The existence of two-dimensional cepstra is shown in [19]. In the appendix of this work a two-dimensional phase-unwrapping technique is introduced based on Tribolet's method [17] for one-dimensional signals. The phase of the cross-spectrum is related to the spatial displacement of spectral energy. If both input images differ only by a lateral displacement, the phase is linear (see (20)). However if the images display other changes besides displacement, such as size and shape changes, the phase terms of the input spectra do not differ just by a linear component.

There are some interesting relations linking inner product, spectrum and moments with each other. Defining the j-k- moment of $\{x(n,m)\}$ as

$$s_{jk} = \sum_{n=0}^{N-1} \sum_{m=0}^{M-1} n^j m^k x(n,m), \tag{21}$$

then the total brightness or luminance mass of the image is given by s_{00}. The center of luminance gravity is derived as

$$\mu_m = \frac{s_{01}}{s_{00}} , \quad \mu_n = \frac{s_{10}}{s_{00}} . \tag{22}$$

The partial derivatives of a two-dimensional spectrum are evaluated as

$$\frac{dX(p,q)}{dp} = DFT\ \{-jnx(n,m)\} = X'_{Rp}(p,q) + jX'_{Ip}(p,q)$$

$$\frac{dX(p,q)}{dq} = DFT\ \{-jmx(n,m)\} = X'_{Rq}(p,q) + jX'_{Iq}(p,q),$$

(23)

with the subscripts R for real part, I for imaginary part, p as derivative with respect to p, and q with respect to q. The derivatives of phase and amplitude then can be derived as

$$\frac{d\ \arg X(p,q)}{dp} = \frac{X_R X'_{Ip} + X'_{Rp} X_I}{X_R^2 + X_I^2}$$

(24)

$$\frac{d\ A_x}{dp} = \frac{X_R X'_{RU} + X_I X'_{IU}}{(X_R^2 + X_I^2)^{\frac{1}{2}}}$$

(25)

(similarly with respect to the variable q). A numerical integration of (24) leads to an approximation of the unwrapped phase. With the spectrum at zero frequencies being purely real, i.e.,

$$X(0,0) = \sum_{n=0}^{N-1} \sum_{m=0}^{M-1} x(n,m)\quad = X_R(0,0) = s_{00}$$

(26)

and its derivative

$$\frac{d\ X(0,0)}{dp} = -j \sum_{n=0}^{N-1} \sum_{m=0}^{M-1} nx(n,m) = -jX'_{IU}(0,0) = -js_{10},$$

(27)

the derivative of the phase at zero frequency is given by

$$\frac{d\ \arg X(0,0)}{dp} = -\frac{X'_{IU}(0,0)}{X_R(0,0)} = -\frac{s_{10}}{s_{00}},$$

(28)

i.e., the phase derivative with respect to p is identical to the negative value of the location of the luminance center of gravity in n-direction. The same holds for the derivative with respect to q, being equal to the negative value of the location in m-direction. Similar results can be derived for the phase of the cross-spectrum. Here the

derivative of the phase at zero frequency is identical to the negative

values of the displacement, i.e., the difference of the position of

the centers of luminance gravity.

As we had seen before, the phase of the cross-spectrum is linear

for images being identical except for lateral displacement. The deriva-

tives then are constant for all frequencies.

It is obvious that the displacement of the center of luminance

gravity is very often a satisfactory indication of moving objects. As

we have shown in this section, this displacement can be evaluated in

the space or frequency domain. The assumption of scene changes con-

sisting solely of lateral displacement, however, has to be judged

carefully for its validity in the case of application being under

research.

CHAPTER 3

IMPROVEMENT OF THE INNER-PRODUCT METHOD

3.1 Problems in the Estimation of Cloud Motion

The inner product method as presented in the previous chapter associates the amount of lateral displacement with the location of the absolute maximum of the inner product of two consecutive images. Cloud size and shape changes, cloud rotation, non-uniformity of wind vectors in different altitudes, to name only few of the typical phenomena the image analyst has to cope with, establish serious limitations to the performance of this estimator [20 - 22]. Whereas in more advantageous situations the absolute value of the inner product maximum is a clear indicator for having matched the same cloud in two consecutive frames, the analysis of more complex scenes might require a separate matching decision prior to the displacement estimation, either by the human operator or a very sophisticated automated computer analysis.

The inner product might not produce meaningful results, if the cloud has undergone severe changes. In those instances we refer to methods introduced in Chapter 4 and 5. Special consideration should be given to the rotation of a cloud, since it often indicates severe weather. Rotation therefore is not regarded as a factor of disturbance but as a parameter to be estimated quantitatively. In these instances it is suggested to estimate the rotation first, then realign both images and employ lateral displacement estimation on the rotation-corrected images.

Rotation could be estimated by an inner product based on a polar-coordinate grid point system centered at the axis of rotation. Since the resulting inner product would be very sensitive to the choice of this axis point, a combined lateral and rotational inner product has to be evaluated until the absolute maximum is found. Notwithstanding the problems of interpolation between the two systems of coordinates, such strategy requires excessive computer power. One of the requirements given for this work, however, was that the developed algorithms were feasible for mini-computers with memory sizes of 64 to 128K byte. This restriction encroaches already on the performance of the Cartesian inner product. The maximum image size available with the equipment used for this work was only 128 by 128 pixels, and even this could be achieved only by a complicated I/O overhead structure and using the image memory for the storage of intermediate results. In the light of the very satisfactory performance of the rotation estimators in Chapter 4 and 5, further consideration is directed now solely towards the improvement of the lateral displacement inner product method.

3.2 Pre-Filtering by Inverse Filters

As we have indicated in the last section, the analysis of cloud motion has to cope with the fact that the objects of interest undergo changes between two consecutive image frames. For the inner product estimator therefore the question arises, how the location of the maximum of the inner product surface is related to the characteristics of the input signals. In other words, how reliable is the inner product method given the fact that mapping the first into the second image is inhomogeneous? Certainly, the more points are mapped by a homogeneous

vector field, i.e., with parallel direction and equal absolute value,
the more energy is concentrated around the maximum peak of the inner
product. As a conclusion, two performance goals of the inner product
method are:

(i) the displacement of only meaningful features should be
estimated,

(ii) the maximum peak of the inner product surface should be as
pronounced as possible, i.e., concentrate as much energy
as possible.

The following paragraphs demonstrate how both tasks can be
achieved simultaneously by a single technique.

A well-known property of the discrete Fourier transform is that,
if a signal is not too severely contaminated by aliasing (i.e., by
undersampling), a 'narrow' inner product peak is equivalent to a
'broad' cross-spectrum, and vice-versa. The limiting case is defined
by the inverse transform of a constant (i.e., 'white') spectrum
$X(p,q) = 1$, for all p,q. The inverse transform of this spectrum
results in an inner product with a single impulse at $\nu = 0$, $\mu = 0$, i.e.,

$$K(\nu,\mu) = \delta(\nu,\mu)$$

with $\delta(.)$ being the unit impulse function

$$\delta(\nu,\mu) = \begin{cases} 1 \text{ for } \nu = 0, \mu = 0 \\ 0 \text{ otherwise.} \end{cases} \tag{29}$$

The inverse transform of a spectrum

$$X(p,q) = \exp\left(-j2\pi\left(\frac{n_0}{N} + \frac{m_0}{M}\right)\right)$$

is the shifted δ-function

$$\delta(\nu - n_0, \mu - m_0) = \begin{cases} 1 \text{ for } \nu = n_0, \mu = m_0 \\ 0 \text{ otherwise.} \end{cases} \tag{30}$$

From a comparison with (20) and (16) it appears that (30) is the inner product of identical signals, each with a white spectrum, shifted laterally by n_0 and m_0.

Since our images of interest, in general, do not possess a white spectrum, we conclude that a narrow inner product peak can be obtained only if the input signals are passed through a 'whitening' filter prior to the inner product operation (Fig. 1).
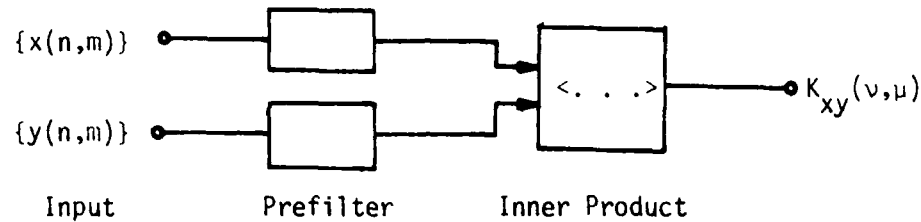
Figure 1. Inner product of pre-filtered images.

A two-dimensional discrete filter is a mapping L which maps an input image $\{x(n,m)\}$ into an output image $\{y(n,m)\} = \{L[x(n,m)]\}$. The response of the filter to the δ-function (29) is called the impulse response or spread function of the filter

$$h(n,m) = L[\delta(n,m)].$$

The output of a linear shift-invariant (LSI) filter is a discrete convolution of input and spread function, i.e.,

$$y(n,m) = \sum_{k=-\infty}^{\infty} \sum_{l=-\infty}^{\infty} x(k,l) \, h(n-k,m-l)$$

$$= \sum_{k=-\infty}^{\infty} \sum_{l=-\infty}^{\infty} x(n-k,m-l) \, h(k,l). \tag{31}$$

The two-dimensional z-transform of an array of complex numbers $f(n,m)$ is defined as [23]

$$F(z_1,z_2) = \sum_{n=-\infty}^{\infty} \sum_{m=-\infty}^{\infty} f(n,m) \, z_1^{-m} z_2^{-n}, \tag{32}$$

where z_1 and z_2 are complex variables. The z-transform evaluated at the surface $z_1 = \exp(j\omega_1)$, $z_2 = \exp(j\omega_2)$, is equal to the (continuous) Fourier transform of $\{f(n,m)\}$ provided this array is absolutely summable. If $\{f(n,m)\}$ is a finite area sequence, the discrete Fourier transform (15) is identical to the Fourier transform evaluated at the frequencies $\omega_1 = 2\pi p/N$ and $\omega_2 = 2\pi q/M$.

The z-transform of the output of a digital LSI filter is given by the product of the z-transforms of input and spread function, i.e.,

$$Y(z_1,z_2) = X(z_1,z_2) \, H(z_1,z_2). \tag{33}$$

The z-transform of the spread function, i.e., $H(z_1,z_2)$ is called the system function. From (33) follows that the desired system function of the inverse filter should be

$$H(z_1,z_2) = \frac{1}{\sum_{n=0}^{N-1} \sum_{m=0}^{M-1} x(n,m) \, z_1^{-n} z_2^{-m}} \tag{34}$$

provided the inverse exists.

A pre-filter designed to improve the detectibility of the inner product maximum peak therefore depends on the spectrum of the input signal. For one-dimensional signals, this approach has been suggested by using various numerical inversion schemes based on the knowledge of the input spectrum [24]. One disadvantage of these techniques is that the spectrum of the signal has to be known a-priori. Furthermore, the pre-filter has to be re-calculated whenever the spectrum of the input changes.

In the following section it will be shown how a two-dimensional discrete filter can be designed with an extended Wiener technique,

approximating the inverse filter to any desired degree. We shall see that a low-order Wiener filter will be a satisfactory approximation for a common class of images, and hence its numerical values will not have to be changed that often. Another feature of this filter is computational efficiency. However before introducing the two-dimensional Wiener filter design technique, some points about the existence of such an inverse filter are in order.

Assume the inverse filter is causal, i.e., its output depends only on the 'present' and 'past' values. This terminology is of course a convention used in the theory of one-dimensional time functions. In this context, 'past,' 'present' and 'future' are defined as orientations in space: past values of $\{x(n,m)\}$ are all values $\{x(k,l)\}$ with $k<n$, $l<m$; future is defined by $k>n$, $l>m$. Call $\{h_c(k,l)\}$, $k\geq 0$, $l\geq 0$, the spread function of this inverse, causal filter. Since the system function (34), in general, is a two-dimensional polynomial of infinite order, the spread function will be of infinite duration:

$$H(z_1,z_2) = \sum_{k=0}^{\infty} \sum_{l=0}^{\infty} h_c(k,l) \, z_1^{-k} \, z_2^{-l}. \tag{35}$$

The filter (35) is called stable [25] if and only if

$$\sum_{k=0}^{\infty} \sum_{l=0}^{\infty} |h_c(k,l)| < \infty. \tag{36}$$

Since the two-dimensional z-transform of any array $f(m,n)$ converges if and only if

$$\sum_{m=-\infty}^{\infty} \sum_{n=-\infty}^{\infty} |f(m,n) \, z_1^{-m} \, z_2^{-n}| < \infty, \tag{37}$$

we conclude that the LSI filter is stable if and only if its system function converges for $|z_1| = |z_2| = 1$.

In one-dimensional systems analysis, the proof of stability generally is established if the poles lie inside the unit circle. From the inversion (34) it is obvious that this is the case whenever the zeros of the signal $x(.)$ lie inside the unit circle, i.e., $x(.)$ is minimum-phase. For one-dimensional functions, the location of the zeros with respect to the unit circle decides whether the signal is minimum-phase, maximum-phase or mixed-phase. Hence for a one-dimensional minimum-phase signal there is a stable, causal inverse filter [26]. If the signal is maximum-phase, i.e., all zeros are outside the unit-circle, a 'left-going' z-transform and an anti-causal system function can be defined to assure stability and convergence.

However a two-dimensional polynomial, in general, cannot be factored into a product of first order polynomials of a single variable, i.e., there is no equivalent decomposition in poles and zeros. The fundamental theorem of algebra does not exist for two-dimensional functions (with the exception of separable functions). The principle of minimum-phase therefore has to be modified for two dimensions [27].

<u>Definition</u>. A sequence $\{x(k,l)\}$ will be called minimum-phase if the following conditions are satisfied:

(1) The two-dimensional z-transform $X(\hat{z}_1,z_2) = 0$, evaluated at any $|\hat{z}_1| = 1$, has no zeros outside the z_2 unit circle.

(2) The two-dimensional z-transform $X(z_1,\hat{z}_2) = 0$, evaluated at any $|\hat{z}_2| = 1$, has no zeros outside the z_1 unit circle.

Stability and minimum-phase then are connected by the following two theorems:

Theorem 1 (Shanks; [27 - 28])

Given that $X(z_1,z_2)$ is a polynomial in (z_1,z_2), for the coefficients of expansion of $1/X(z_1,z_2)$ in negative powers of z_1 and z_2 to converge absolutely, it is necessary and sufficient that $X(z_1,z_2)$ not be zero for $|z_1|$ and $|z_2|$ simultaneously greater than one.

Theorem 2 (Shanks [27])

A sequence $\{x(n,m)\}$ is two-dimensionally minimum-phase if and only if the polynomial $X(z_1,z_2) = 0$ has no zeros for which $|z_1| \geq 1$ and $|z_2| \geq 1$ simultaneously.

From Theorems 1 and 2 it can be concluded that the inverse filter $H(z_1,z_2) = 1/X(z_1,z_2)$ is stable if $X(z_1,z_2)$ is minimum-phase. If $X(z_1,z_2)$ is not minimum-phase, then $H(z_1,z_2)$ will not be stable.

However if $X(z_1,z_2)$ is maximum-phase, there is a stable inverse filter

$$H(z_1,z_2) = \sum_{k=0}^{\infty} \sum_{l=0}^{\infty} h_a(k,l) \, z_1^k \, z_2^l \tag{38}$$

with $h_a(k,l)$ the anti-causal or anticipatory impulse response. The output of this filter depends on present and future input values. Whereas in the analysis of time-varying functions future values are not always available, anti-causal system functions do not lead to any problem in image processing as long as the complete image is available at the time of processing.

Since cloud images are generally mixed phase type of signals, the spread function of a stable inverse filter will be both causal and anti-causal, i.e.,

$$H(z_1,z_2) = \sum_{k=-\infty}^{\infty} \sum_{l=-\infty}^{\infty} h(k,l) \, z_1^{-k} \, z_2^{-l}. \tag{39}$$

The output sequence therefore will be given by a double-sided convolution

$$y(n,m) = \sum_{k=-\infty}^{\infty} \sum_{l=-\infty}^{\infty} h(k,l)\ x(n-k,m-l).$$ (40)

Note that the input sequence is of finite area, the double sum therefore will actually have finite boundaries.

In general it will not be possible to find a finite (i.e., realizable) filter that exactly inverts the spectrum of the input signal. Our goal therefore consists of finding a filter that approximates the inversion according to some criterion of optimality. Our choice of filter-type is guided by the convolution (40) and its advantages of computational implementation. Furthermore we are guaranteed to obtain a stable filter. The input-output relationship of such a finite impulse response (FIR) filter is

$$y(n,m) = \sum_{k=-K}^{K} \sum_{l=-L}^{L} a(k,l)\ x(n-k,m-l)$$ (41)

with $a(.)$ the causal/anti-causal spread function. Note that we expect the values of $a(k,l)$ be different from the low-order terms of the spread function $\{h(k,l)\}$ of the exact inversion. In the next section it is shown how the desired filter coefficients $\{a(k,l)\}$, $-K \leq k \leq K$, $-L \leq l \leq L$, can be derived by a least-squares minimization technique.

3.3 Design of the Planar Least Squares Inverse Filter

In general, it will not be possible to find a filter (41) that produces exactly the desired unit pulse image with a white spectrum. The objective of this section is to find filter coefficients $\{a(k,l)\}$ $-K \leq k \leq K$, $-L \leq l \leq L$, such that its output approximates the unit pulse array

$\delta(n,m)$ in the least squares sense. This approximation method was developed by Gauss and successfully applied in one-dimensional signal processing [29]. In the sequel it will be shown how this technique can be extended to a two-dimensional (i.e., planar) least squares inverse (PLSI) filter. Since the least-squares design technique is often confused with the so-called Wiener filter design method, it should be noted that the former is not based on any statistical assumptions, whereas the latter requires the estimation or a-priori knowledge of spatial correlation functions [30, p. 228].

The PLSI filter can be thought of as a cancellation or prediction error filter [31, 32]

$$y(n,m) = x(n,m) - \sum_{\substack{k=-K \\ (k,l)\neq(0,0)}}^{K} \sum_{l=-L}^{L} b(k,l)\, x(n-k,m-l) \qquad (42)$$

with the prediction filter coefficients $b(k,l)$. Comparing this notation with the filter (41), one can see that

$a(0,0) = 1$

$a(k,l) = -b(k,l)$ for $(k,l) \neq (0,0)$. $\qquad (43)$

Recall that we require $y(n,m) = \delta(n,m)$. Hence it is reasonable to require $y(0,0) = x(0,0)$ and $y(k,l)$ for $(k,l) \neq (0,0)$ as small as possible. With the total squared error thus being

$$E = \sum_{n=1}^{\infty} \sum_{m=1}^{\infty} (y(n,m))^2, \qquad (44)$$

the filter coefficients are obtained by minimizing E with respect to each coefficient $a(k,l)$. With (42) and (43) the error (44) becomes

$$E = \sum_{n=1}^{\infty} \sum_{m=1}^{\infty} \left(\sum_{k=-K}^{K} \sum_{l=-L}^{L} a(k,l)\, x(n-k,m-l) \right)^2$$

$$= \sum_{k=-K}^{K} \sum_{l=-L}^{L} \sum_{h=-K}^{K} \sum_{i=-L}^{L} a^*(k,l) \, a(h,i) \cdot$$

$$\sum_{n=1}^{\infty} \sum_{m=1}^{\infty} x(n-k,m-l) \, x(n-h,m-i), \tag{45}$$

with * denoting the complex conjugate. Since the double sum

$$\sum_{n=1}^{\infty} \sum_{m=1}^{\infty} x(n-k,m-l) \, x(n-h,m-i)$$

is the inner product $K_{xx}(h-k,i-l)$, (45) can be written as

$$E = a^*(-K,-L) \sum_{h=-K}^{K} \sum_{i=-L}^{L} a(h,i) \, K_{xx}(h+K,i+L) + \ldots$$

$$+ a^*(0,0) \sum_{h=-K}^{K} \sum_{i=-L}^{L} a(h,i) \, K_{xx}(h,i) + \ldots$$

$$+ a^*(K,L) \sum_{h=-K}^{K} \sum_{i=-L}^{L} a(h,i) \, K_{xx}(h-K,i-L). \tag{46}$$

Setting the derivatives of (46) with respect to the filter coefficients

$a(f,g)$ to zero, we obtain the system of equations

$$\sum_{k=-K}^{K} \sum_{l=-L}^{L} a(k,l) \, K_{xx}(k-f,l-g) = 0 \ \text{for} \ \left\{ \begin{matrix} -K \leq f \leq K \\ -L \leq g \leq L \\ \text{but } (f,g) \neq (0,0) \end{matrix} \right\} \tag{47}$$

Inserting (47) into (46), the minimal error becomes

$$E_{min} = \hat{e} = \sum_{k=-K}^{K} \sum_{l=-L}^{L} a(k,l) \, K_{xx}(k,l). \tag{48}$$

Equations (47) and (48) are the two-dimensional normal equations. In

matrix form they can be written as

$$\begin{pmatrix} R_0 & R_{-1} \cdots\cdots R_{-L} \cdots\cdots\cdots\cdots R_{-2L} \\ R_1 & R_0 \\ \vdots \\ R_L \cdots\cdots\cdots\cdots R_0 \cdots\cdots\cdots\cdots R_{-L} \\ \vdots \\ R_{2L} \cdots\cdots\cdots\cdots R_L \cdots\cdots\cdots\cdots R_0 \end{pmatrix} \begin{pmatrix} \underline{a}_L \\ \underline{a}_{L-1} \\ \vdots \\ \underline{a}_\zeta \\ \vdots \\ \underline{a}_{-L} \end{pmatrix} = \underline{\zeta} \qquad (49)$$

with R_j being the Toeplitz sub-matrix

$$R_j = \begin{pmatrix} K_{xx}(0,j) \cdots\cdots K_{xx}(-K,j) \cdots\cdots\cdots K_{xx}(-2K,j) \\ \vdots & \vdots & \vdots \\ K_{xx}(K,j) \cdots\cdots K_{xx}(0,j) \cdots\cdots\cdots K_{xx}(-K,j) \\ \vdots & \vdots & \vdots \\ K_{xx}(2K,j) \cdots\cdots K_{xx}(K,j) \cdots\cdots\cdots K_{xx}(0,j) \end{pmatrix} \qquad (50)$$

the sub-vectors of filter coefficients

$$\underline{a}_j = \begin{pmatrix} a(K,j) \\ a(K-1,j) \\ \vdots \\ a(0,j) \\ \vdots \\ a(-K,j) \end{pmatrix} \qquad (51)$$

and the vector $\underline{\zeta}$ is a column vector containing zero elements except for the minimal error $\hat{e}$ in the position corresponding to $a(0,0)$:

$$\underline{\zeta} = \begin{pmatrix} 0 \\ \vdots \\ 0 \\ \hat{e} \\ 0 \\ \vdots \\ 0 \end{pmatrix} \qquad (52)$$

Since the filter coefficients have to be normalized such that $a(0,0) = 1$, the value $\hat{e}$ in (52) can be replaced by a 1. The solution for the optimum filter coefficients is simply achieved by taking the middle column of the inverse of the R - matrix in (49) and equating it to the filter coefficients of the a-vector in (49). Since the R-matrix of (49) is block-Toeplitz, its inversion can be done recursively by a modified Levinson algorithm [57]. The predictor filter coefficients $\{b(k,l)\}$ of (42) then are obtained as

$$b(j,k) = -a(j,k)/a(0,0). \tag{53}$$

As a special case consider the class of images with an exponential inner product of the form

$$K_{xx}(n,m) = K_{xx}(0,0) \, \rho^{|n-m|} \tag{54}$$

with ρ a constant such that $0 \le \rho \le 1$.

These images are usually referred to as first-order Markov processes, although a strict definition would require the replacement of the inner product by the spatial correlation function [30, p. 108]. The constant ρ is the 'correlation' of adjacent pixels in rows and columns.

Real-world images approximate the Markov property quite frequently [33]. The inner product sequence is a Toeplitz matrix and bears the advantage of easy diagonalization and approximation to a circulant matrix. A whitening filter for such a Markovian image then is a function of the single parameter ρ. With the technique of solving the normal equations (49), a filter of order 3 x 3 results in the matrix of filter coefficients

$$[a(j,k)] = \begin{pmatrix} a(1,1) & a(1,0) & a(1,-1) \\ a(0,1) & a(0,0) & a(0,-1) \\ a(-1,1) & a(-1,0) & a(-1,-1) \end{pmatrix} = \begin{pmatrix} \rho^2 & -\rho(1+\rho^2) & \rho^2 \\ -\rho(1+\rho^2) & (1+\rho^2)^2 & -\rho(1+\rho^2) \\ \rho^2 & -\rho(1+\rho^2) & \rho^2 \end{pmatrix}$$

$$(55)$$

For $\rho = 1$, i.e., high adjacent 'correlation,' the filter (55) reduces to the Laplacian edge enhancement filter [11, p. 482]

$$[a(j,k)] = \begin{pmatrix} 1 & -2 & 1 \\ -2 & 4 & -2 \\ 1 & -2 & 1 \end{pmatrix}$$

$$(56)$$

At this point some comments about the connection between inverse filtering and edge detection are in order. Since many actual images display a high amount of energy in the lower spatial frequencies, as long as the signal-to-noise ratio is sufficiently high, we expect an inverse filter to have high-pass characteristics. However, the high-frequency energy of images is usually due to sudden changes of the brightness value, as in edges etc.

The inner product between two different cloud images that are processed through such a filter then is based more on the high-frequency energy of the input signals, proportional to the order of the filter.

The notion of lateral displacement estimation based on the high-frequency information had been discovered earlier and leads to the suggestion of passing the images through high-pass filters prior to the inner product operation [14, 20, 34]. The technique described in this section, however, adapts itself to the images under consideration and leads to a filter in the least squares optimum sense.

The importance of edges, contours and texture as reference marks for the estimation of cloud displacement has been sta. ! before [4].

As we shall see in the next section, the inner product of a pre-filtered set of images leads to a better maximum peak performance, as long as the displacement of the high-frequency image contents is rather homogeneous. If this is not the case, i.e., if no part of the high-frequency information can be matched with any other part of the second input frame, the method described above might not lead to any significant maximum at all. In many cases of practical interest, however, the change of cloud shape occurs only in some parts. The inner product of pre-filtered images then would indicate the displacement of those high-frequency parts that have translated in a more homogeneous fashion.

3.4 Results

To demonstrate the effect of inverse pre-filtering on the inner product surface, three pairs of consecutive cloud images were chosen with various degrees of changes (Fig. 2(a-f)). The cloud pair I of Fig. 2(a-b) shows almost no changes besides lateral translation. Cloud pair II (Fig. 2(c-d) reveals substantial size and shape changes in the North-East section of the cloud. Image pair III of Fig. 2(e-f) consists of a field of loosely connected clouds with a rather fuzzy appearance.

The inner product surfaces were obtained as follows. Upon inspection of the histogram of the given images, a threshold was selected and the background removed by subtraction. It should be noted that in the case of infrared (IR) imagery, the removal of dark background areas is equivalent to the specification of a temperature (and thus, in general, an altitude) level. Subsequent estimation of lateral cloud displacement then would be based on the information corresponding to

Fig. 2 (a,b). Cloud pair I.

Fig. 2 (c,d). Cloud pair II.

Fig. 2 (e,f). Cloud pair III.
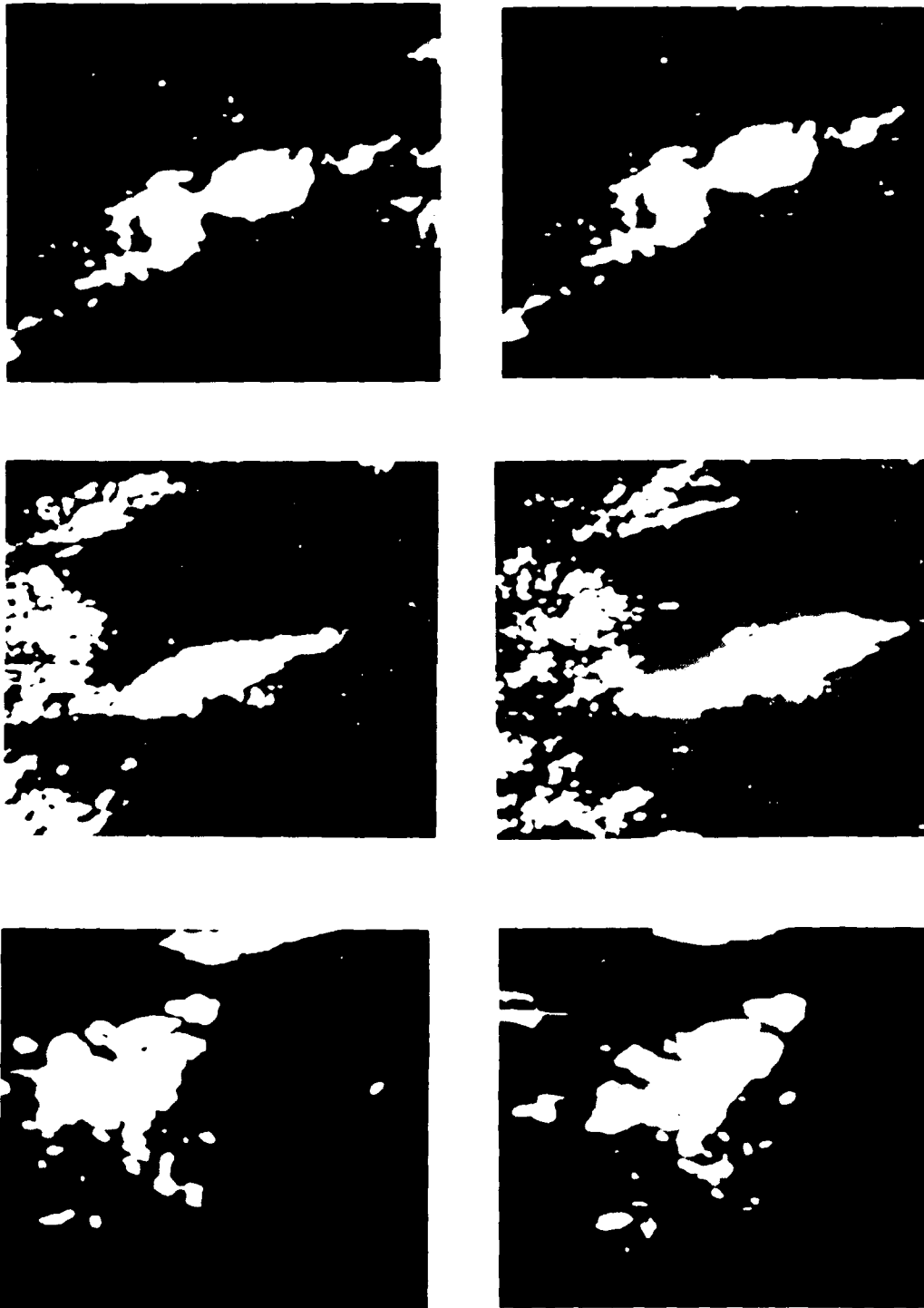
Figure 2. Examples of consecutive cloud images used in the text.

temperature lower than the given threshold, i.e., for higher clouds.

A 3 x 3 inverse filter then was derived by solving the normal equations (49). As indicated in the preceding section, the filter coefficients were normalized such that $a(0,0) = 1$.

The input images were pre-filtered by a direct implementation of the convolution (41). Subsequently the inner product was calculated by the fast Fourier transform (FFT) method. Since the equipment available for this operation consisted of a PDP 11/60 mini-computer and a single-frame Ramtek 9050 display processor, the size of in-core memory was severely limited. Therefore a two-dimensional FFT program was written that makes use of the Ramtek image memory for the storage of intermediate floating-point values and thus avoids time-consuming I/O operations with mountable storage devices. With this configuration a maximum image size for the inner product of 128 x 128 was achieved.

Since the process of pre-filtering might result in negative pixel values, a constant bias was added and later, during the inner product operation, subtracted again.

In Fig. 3(a-c) the inner product surfaces are presented without prior inverse filtering; Fig. 3 a corresponds to the image pair I, Fig. 3 b to pair II and Fig. 3 c to image pair III. The smoothness of the surface is clearly discernible. In spite of the fact that the location of the maximum peak can be evaluated numerically, its interpretation as a meaningful displacement estimate, however, remains questionable.

The inner product surfaces in Fig. 4 (a-c) are the equivalent results when pre-filtering with a 3 x 3 PLSI filter is performed prior to the inner product operation. In Table 1 the respective (auto) inner

Fig. 3 (a)
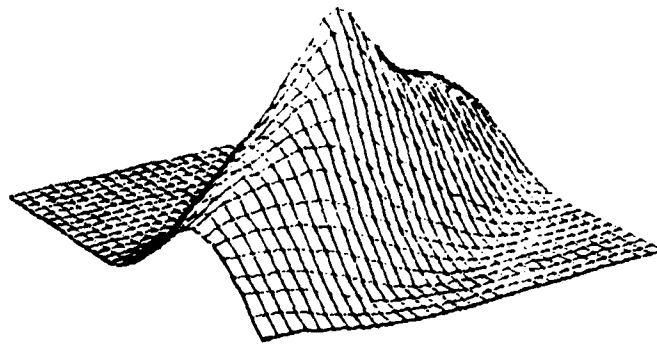
Fig. 3 (b)
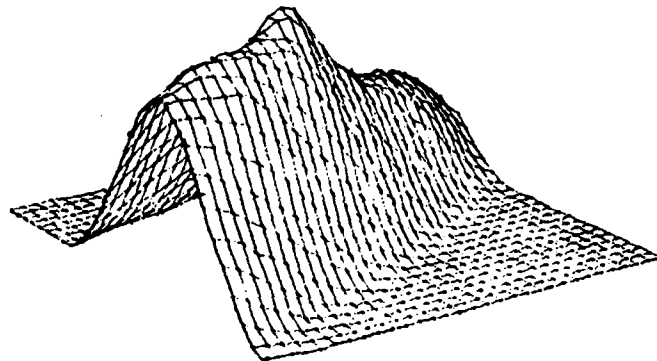
Fig. 3 (c)
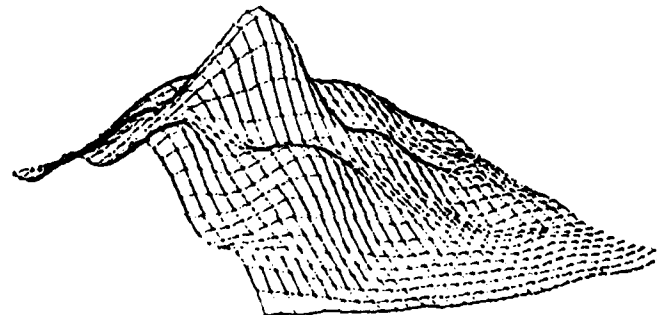
Figure 3. Inner product surfaces without pre-filtering.

Fig. 4 (a)
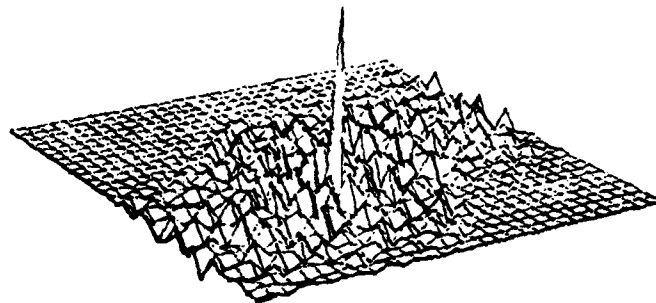
Fig. 4 (b)
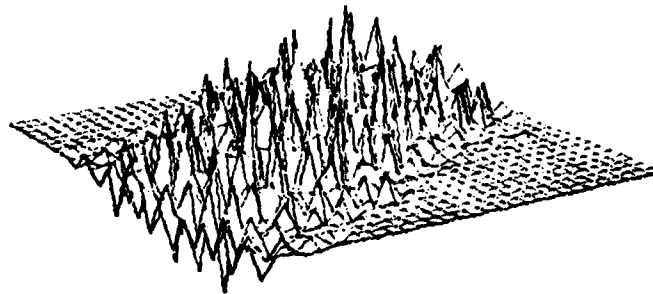
Fig. 4 (c)
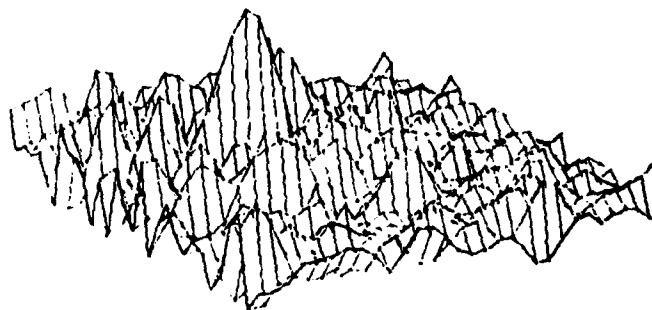
Figure 4. Inner product surfaces after PLSI pre-filtering.

Table 1. Inner product surfaces K_{xx} (ν,μ).

		Image: Fig. 2 (a)		
0.2287	0.3712	0.5451	0.7037	0.7883
0.4096	0.6014	0.7875	0.8755	0.8006
0.6325	0.8319	1.0000	0.8319	0.6325
0.8006	0.8755	0.7875	0.6014	0.4096
0.7883	0.7037	0.5451	0.3712	0.2287

		Image: Fig. 2 (c)		
0.5319	0.5943	0.6504	0.6720	0.6582
0.6269	0.7335	0.8201	0.8085	0.7336
0.7237	0.8771	1.0000	0.8771	0.7237
0.7336	0.8085	0.8201	0.7335	0.6269
0.6582	0.6720	0.6504	0.5943	0.5319

		Image: Fig. 2 (e)		
0.5309	0.6001	0.6559	0.6502	0.6086
0.6617	0.7755	0.8490	0.8012	0.7021
0.7470	0.9025	1.0000	0.9025	0.7470
0.7021	0.8012	0.8490	0.7755	0.6617
0.6086	0.6502	0.6559	0.6001	0.5309

product surface $K_{xx}(\nu,\mu)$ around the center $(\nu,\mu) = (0,0)$ is shown. The
values are normalized with respect to $K_{xx}(0,0)$ such that the affinity
of the given images to the Markov processes (54) can be established.
The 3 x 3 inverse filter coefficients are listed in Table 2.

Although the maximum peak of Fig. 4 (a) is much more pronounced
than in Fig. 3(a) for cloud pair I, the same cannot be said for cloud
pair II. As Fig. 4(b) shows, the method of pre-filtering can result in
a multitude of relative maxima. Although the location of the absolute
maximum is still in the vicinity of the maximum of Fig. 3(b), such a
result does not necessarily increase our confidence in the practicability

Table 2. PLSI filter coefficients.

$$\begin{bmatrix} a(1,1) & a(1,0) & a(1,-1) \\ a(0,1) & a(0,0) & a(0,-1) \\ a(-1,1) & a(-1,0) & a(-1,-1) \end{bmatrix}$$

Image: Fig. 2(a)

0.223	-.471	0.086
-.338	1.000	-.338
0.086	-.471	0.223

Image: Fig. 2(c)

0.136	-.247	0.046
-.444	1.000	-.444
0.046	-.247	0.136

Image: Fig. 2(e)

0.249	-.440	0.137
-.445	1.000	-.445
0.137	-.440	0.248

as an estimator for lateral displacement. The link between high-pass filtering, inverse filtering and edge enhancement was established in the previous section. The result of Fig. 4(b) then can be interpreted as follows. Since the cloud has undergone a significant change in some areas, the inner product of the high-frequency segments of the signal (such as edges and texture) indicate relative match at several vectors of displacement. In other words, if the displacement of the high-frequency parts is not homogeneous, the number of relative maxima will increase. A similar result can be seen in Fig. 4(c) for cloud pair III. Although the displacement has occurred in a more homogeneous

fashion (resulting in a more pronounced absolute maximum), the quali-
tative effect is the same.

As a solution to the foregoing problem, the following modifica-
tion of the filter coefficients is suggested. The coefficients $a(k,l)$
for all indices besides $(0,0)$ are pre-multiplied by a factor c with
$0 \leq c \leq 1$. This factor determines the amount of the original image added
to the pre-filtered output. In essence the frequency characteristic
of the filter changes from high-pass to high-emphasis. For $c = 0.5$,
the filter output will consist of the normalized sum of the filtered
image and the original input. In other words, the choice of the empha-
sis factor c determines how much energy of the lower frequency range
is to be subjected to the inner product operation.

In Fig. 5(a-c) an emphasis factor of 0.75 was chosen. This
allows the additional leakage of 25% of the lower frequencies into the
maximum peak of the inner product surface. The results therefore rep-
resent a compromise between maximum peak sharpness and detectibility.

The numerical location of the absolute maximum of the inner
product surface plots is listed in Table 3. Since each maximum falls
on a discrete grid point, a quadratic surface is fit to the discrete
inner product values around the maximum and a search is done to find
the location of the maximum of the continuous quadratic surface.

Since the grid points of the satellite images under study are
spaced with an equivalent surface distance of 5 . . . 20 km, a high
accuracy in the determination of the maximum is desired. For example
it is desired to estimate wind speeds from cloud displacement with an
accuracy of $\pm$ 3 m/sec.

Fig. 5(a)
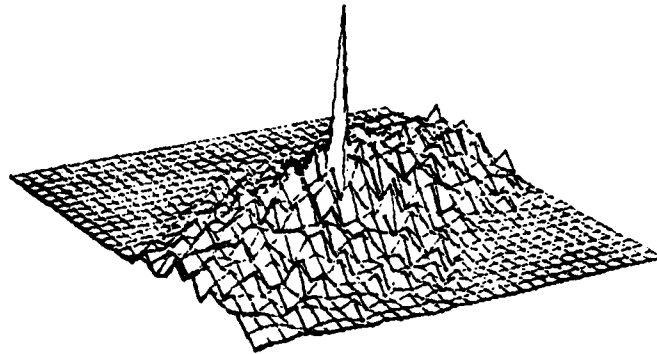
Fig. 5(b)
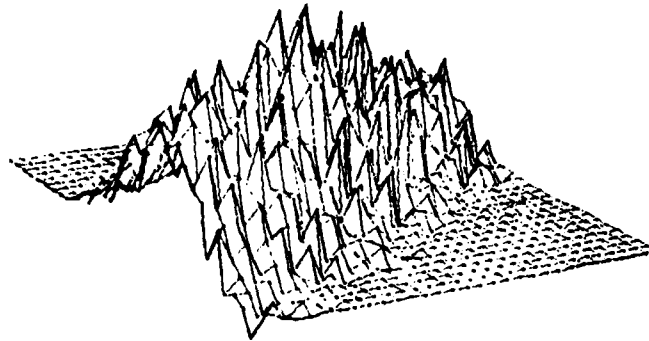
Fig. 5(c)
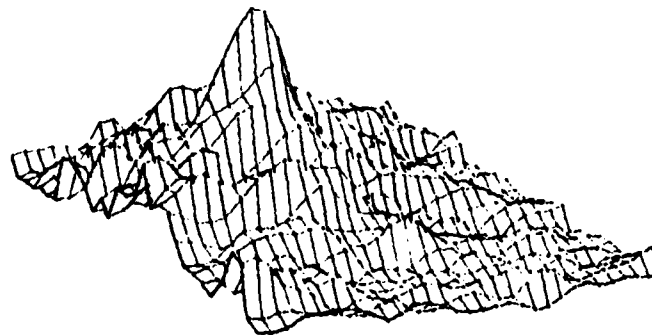
Figure 5. Inner product surfaces with PLSI pre-filter and emphasis
factor c = 0.75.

Table 3. Displacement estimates including quadratic interpolation (in pixel units).

Cloud Pair	I		II		III	
	Δn	Δm	Δn	Δm	Δn	Δm
no pre-filter	-2.0	1.2	2.5	0.6	2.8	4.1
PLSI pre-filter	-1.9	1.2	-3.1	2.0	4.1	4.0
PLSI pre-filter with emphasis factor $c = 0.75$	-1.8	1.1	1.75	0.8	4.2	3.7

3.5 Summary

This chapter dealt with the improvement of the maximum peak detectibility of the inner product as lateral displacement estimator for clouds. Since a narrow inner product peak is equivalent to a broad cross-spectrum, pre-filtering with an inverse filter is suggested prior to the inner product operation. For a filter order much lower than the image size, only an approximation of the inverse can be achieved. The design of the (two-dimensional) planar least squares inverse (PLSI) filter is introduced. Since clouds are usually mixed-phase signals, the optimum filter is not causal. This does not lead to any problems in digital image processing. The filter coefficients are obtained by solving the normal equations extended for two dimensions. In general, the pre-filter obtains high-pass characteristic and thus emphasizes edges and the texture of cloud. It can be shown that a 3 x 3 filter designed for an image with exponential inner product is equal to an edge detector found in the literature.

The method of PLSI pre-filtering is demonstrated by 3 examples of consecutive cloud images. As long as the pattern of the high-frequency information does not change drastically, very good results

can be achieved. Otherwise it is suggested to modify the filter coefficients by multiplication with a constant factor. This changes the frequency characteristic of the filter from high-pass to high-emphasis. The choice of the factor determines the amount of lower frequencies exercising influence on the build-up of the maximum peak. Thus a compromise between peak detectibility and sharpness can be achieved. To further improve the identification of the location of the maximum peak, the inner product around the obtained discrete maximum value is fit to a quadratic surface, and its maximum searched for.

CHAPTER 4

BIVARIATE NORMAL FIT

4.1 Introduction

From the results of the foregoing chapter it becomes apparent
that the inner product method for lateral displacement estimation does
not perform satisfactorily, if the cloud scene has undergone severe
changes of its shape. The same problem arises when the cloud rotates,
either by horizontal shear or due to a curved track. Since the inner
product in the form presented in this work is based on a summation of
cross-energy along the Cartesian system of coordinates, any rotation
of the input images cannot be accounted for. Not only would the degre-
dation of the maximum peak indicate a mis-match, but its location would
also be, in general, a biased estimate of the purely lateral displace-
ment.

Another point of inconvenience stems from the large amount of
computer memory and the inherently long CPU time required to evaluate
the inner product. The calculation of a single inner product surface
of the size 32 x 32 grid points from images of the size 128 x 128 takes
on the PDP 11/60 typically 15-20 minutes (pre-filtering included).
However it is believed that a much faster performance could be achieved,
if special function processors were incorporated in the computer
hardware. If these constraints cannot be met, new displacement esti-
mators have to be developed. These estimators then should:

--identify cloud size changes quantitatively

--identify lateral translation

--identify rotation

--perform fast in a mini-computer environment.

The estimator introduced in this chapter is based on fitting the luminance values of the cloud scene (a single cloud or a cloud field) to a bivariate normal (Gaussian) distribution. The proposed procedure is very fast and yet delivers accurate information on lateral displacement, rotation, and size changes.

4.2 Theory

The luminance or brightness values $\{x(n,m)\}$ of a cloud image can be fit to a bivariate normal density surface placed over the center of luminance gravity, defined as

$$f(\tilde{n},\tilde{m}) = B \exp\left\{-\frac{1}{2(1-r^2)} \left[\frac{(\tilde{n}-\mu_n)^2}{\sigma_n^2} - 2r\frac{(\tilde{n}-\mu_n)(\tilde{m}-\mu_m)}{\sigma_n\sigma_m} + \frac{(\tilde{m}-\mu_m)^2}{\sigma_m^2}\right]\right\} \quad (57)$$

with

$$B = \frac{1}{2\pi\sigma_n\sigma_m\sqrt{1-r^2}}, \quad (58)$$

μ_n and μ_m, the center of luminance gravity (22), and the second-order central moments

$$\sigma_n^2 = \frac{1}{s_{oo}} \sum_{n=0}^{N-1} \sum_{m=0}^{M-1} (n - \mu_n)^2 \, x(n,m)$$

$$\sigma_m^2 = \frac{1}{s_{oo}} \sum_{n=0}^{N-1} \sum_{m=0}^{M-1} (m - \mu_m)^2 \, x(n,m)$$

$$r = \frac{1}{s_{oo}\sigma_n\sigma_m} \sum_{n=0}^{N-1} \sum_{m=0}^{M-1} (n - \mu_n)(m - \mu_m) \, x(n,m), \quad (59)$$

with s_{00} the total luminance mass of the image. Note that $f(\tilde{n},\tilde{m})$ is defined on the continuous $\tilde{n},\tilde{m}$ plane, the image $\{x(n,m)\}$ however is given on its integral grid points. The term of (57) enclosed by the square brackets indicates that the locus of points in the continuous $\tilde{n},\tilde{m}$ plane such that the density is constant, i.e., $f(\tilde{n},\tilde{m}) = c_1$, is an ellipse of the normal form

$$\frac{(\tilde{n} - \mu_n)^2}{\sigma_n^2} - \frac{2r(\tilde{n} - \mu_n)(\tilde{m} - \mu_m)}{\sigma_n \sigma_m} + \frac{(\tilde{m} - \mu_m)^2}{\sigma_m^2} = c_2, \qquad (60)$$

with its center (μ_n, μ_m) as in Fig. 6. The density $f(\tilde{n},\tilde{m})$ is maximum at this center, and it equals

$$f(\mu_n, \mu_m) = B, \qquad (61)$$

with B as defined in (58).

If $c_2 = 1$, then for $f(\tilde{n},\tilde{m}) = f(\mu_n,\tilde{m})$,

$$(m - \mu_m)^2 = \sigma_m^2,$$

and for $f(\tilde{n},\tilde{m}) = f(\tilde{n},\mu_m)$,

$$(n - \mu_n)^2 = \sigma_n^2.$$

That is, the radii of the ellipse parallel to the coordinate axes are equal to σ_n and σ_m (see Fig. 6). If $r = 0$, then the principle axes of the ellipse are parallel to the coordinate axes. A cloud or cloud field is fit to a bivariate normal density by calculating the moments and central moments of the image brightness and equating them with the moments that define the normal distribution of luminance values. Changes of the parameters of the ellipse indicate rotation, lateral displacement and size changes as long as those are reflected by changes of the major and minor axis (denoted by a and b in Fig. 6).

a = major axis
b = minor axis
σ = angle of inclination
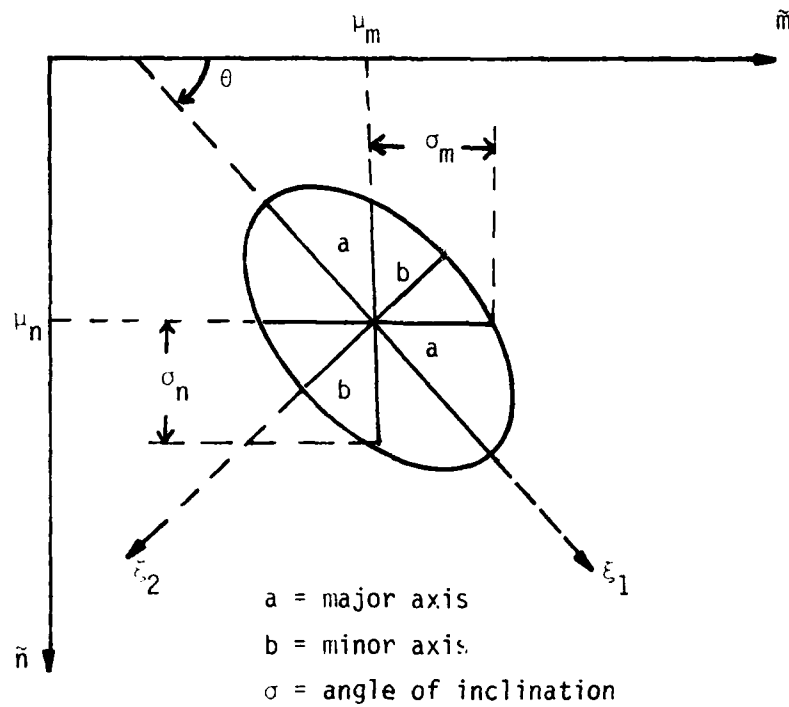
Figure 6. Ellipse of constant normal density for $c_2 = 1$.

A combination of this process and the inner product method can be developed, where the rotation is estimated first by identifying the rotation of the ellipse. The input images then are rotationally re-aligned, and subsequently the inner product method is employed for a more accurate estimation of the lateral displacement.

Once the moments of the cloud scene are established, the length of the principle axes and the angle of inclination θ of the ellipse can be determined as follows:

We introduce a new Cartesian system of coordinates placed over the center of the ellipse,

$$\xi_1 = (\tilde{n} - \mu_n) \sin\theta + (\tilde{m} - \mu_m) \cos\theta$$
$$\xi_2 = (\tilde{n} - \mu_n) \cos\theta - (\tilde{m} - \mu_m) \sin\theta,$$

(62)

with ξ_1 parallel to the major axis a, and ξ_2 parallel to the minor axis b (see Fig. 6). Within this new system, the coefficient r (see (59)) should be equal to zero, i.e.,

$$\sum_{\xi_1=-\infty}^{\infty} \sum_{\xi_2=-\infty}^{\infty} \xi_1 \xi_2 \; x(\xi_1,\xi_2) = 0. \tag{63}$$

With (62), $x(\xi_1,\xi_2)$ can be expressed in terms of $\bar{n},\bar{m}$ and (63) becomes

$$\sin\alpha \cos\alpha \; \sigma_n^2 + r(\cos^2\alpha - \sin^2\alpha)\sigma_n\sigma_m - \sin\alpha \cos\alpha \; \sigma_m^2 = 0.$$

Hence,

$$\alpha = \tfrac{1}{2} \tan^{-1} \frac{2\, r\sigma_n\sigma_m}{\sigma_n^2 - \sigma_m^2} \tag{64}$$

The length of major and minor axis can be obtained by solving the following equations.

At first, from the properties of the radii of an ellipse it follows that

$$a^2 + b^2 = \sigma_n^2 + \sigma_m^2. \tag{65}$$

Furthermore, the pre-factor B of (57) must be the same in the ξ_1,ξ_2 system, i.e.,

$$\frac{1}{2\pi\sigma_n\sigma_m \sqrt{1 - r^2}} = \frac{1}{2\pi ab}$$

or

$$a\,b = \sigma_n\sigma_m \sqrt{1 - r^2} \tag{66}$$

Now (65) and (66) are two equations that can be solved for a and b. Note that

$$\left.\begin{array}{l} a + b > 0: \text{ for any case} \\ a - b > 0: \text{ for } r > 0 \\ a - b < 0: \text{ for } r < 0. \end{array}\right\} \tag{67}$$

4.3 Examples

One of the operational differences between the inner-product method and the method of tracing ellipses of constant gray-value distribution is that the latter requires the 'man-in-the-loop' to determine the same cloud or cloud field on both input images. Whereas the maximum of the inner product can be used as a criterion for the matching condition, the bivariate normal fit requires this information a-priori. The method is applied best in an interactive type of operation. The cloud analyst selects a cloud of interest. From the evaluation of the histogram he determines a threshold and positions a frame around the target cloud. The computer program then is envoked in order to obtain the parameters of the ellipse for the gray values within the selected frame. The results are obtained numerically as well as utilized for an overlay on top of the cloud image (see Fig. 7).

Figure 7. Ellipse of constant gray-value density as overlay on cloud image. Elliptic parameters are determined for gray values within the interactively selected frame.

A time series of these parameters then is established by analyzing a sequence of images. An evaluation of this time series might support motion analysis and facilitate the prediction of the elliptic parameters.

As an example we considered the cloud pairs of Fig. 2. The parameters of the ellipses are listed in Table 4. The resulting values for the lateral displacement (i.e., the displacement of the center of luminance gravity) should be compared with Table 3. As one might expect, the results are rather close for the case of the cloud with only few changes. In the assessment of the other cases one should keep in mind that the number of computations of the bivariate-fit method is considerably lower than for the inner-product method. With the PDP 11/60 equipment described in the previous chapter, the results for a 128 x 128 image are obtained in typically 5 . . . 10 seconds.

4.4 Summary

In this chapter a method was introduced that delivers not only estimates of the lateral displacement vector, but also of rotation and size changes. These parameters are obtained from fitting a bivariate normal surface to the luminance values of a cloud or a cloud field. By tracing only the ellipses of constant density, motion vectors and distribution changes are identified. Compared with the inner-product method, this technique not only delivers additional information on the cloud, but can also be applied for whole cloud fields, in particular if the geometric lay-out of the scene is somewhat elliptic. This method is also much faster than the inner-product technique and requires considerably less memory allocation. However it requires the a-priori information of match by the human operator.

Table 4. Elliptic parameters for images of Fig. 2.

	μ_n, μ_m center of ellipse (pixel units)		θ inclination in degrees	a major axis in pixel units	b minor
Cloud Pair I:					
Fig. 2 (a)	180.2	314.6	24.3	10.8	4.2
Fig. 2 (b)	178.0	316.1	24.0	11.1	4.1
Difference	- 1.8	1.5	- 0.3	0.3	-0.1
Cloud Pair II:					
Fig. 2 (c)	214.0	185.8	27.30	12.2	3.8
Fig. 2 (d)	221.6	184.4	24.34	19.2	4.6
Difference	7.6	- 0.6	- 2.96	7.0	0.8
Cloud Pair III:					
Fig. 2 (e)	325.5	135.0	- 4.64	14.1	10.0
Fig. 2 (f)	336.8	137.1	- 3.04	20.1	12.1
Difference	11.3	2.1	- 1.60	6.1	2.1

CH 5

FOURIER DESCRIPTORS AND ELLIPTIC APPROXIMATION
OF CLOUD CONTOURS

5.1 Introduction

The approaches taken in the previous two chapters demonstrate
the fact that any method of motion analysis is based on a particular
model relating the given image to a meaningful description of the pic-
torial information. As we have seen, the inner-product method is
originally based on the distribution of the signal energy. The pre-
filter, however, operates as an edge-enhancer and thus shifts the
emphasis to the information embedded in the edges and contours.

The method described in the previous chapter is based on the
derivation of a simple geometric planar curve, the ellipse, from the
distribution of luminance values and a subsequent analysis of the
parameters of this ellipse.

In this chapter now we shall depart one step further away from
the gray level information of the image by introducing a parametric
description of closed contours. The only remaining link to the gray
level information consists of the fact that the contour is defined as
the line of constant gray level. In the case of visible data, the
contour could be defined by a gray level slightly higher than the dark
background, if the whole cloud is to be encompassed. In the case of
IR imagery, the pixel luminance represents temperature and usually can

be associated with altitude. Hence a contour could be defined at a particular temperature of interest.

Many times it is possible to find distinct contours even in situations where the clouds are not clearly separated. This feature could be employed by the cloud analyst who wants to focus on isolated phenomena like overshooting cloud tops. After having analyzed the histogram of that particular area, he selects a threshold and obtains a contour around an area with temperature values relatively lower than outside the boundary.

Recent research [35 - 41] provides evidence that the Fourier descriptor (FD) is a simple and precise method for describing and comparing the contours of closed, planar figures. Common to all cited publications is the derivation of a functional description of the given contour and its subsequent Fourier series (FS) expansion. Interpretation and analysis of the contour then is performed in the frequency domain.

With respect to the functional description of the contour in the image plane, two types of FD's have been developed. The older method [36,37] is based on a normalized angle versus arclength function. In spite of its fast matching algorithm, its practicability is limited for several reasons. First, due to the normalization process in the image domain, the resulting FD does not contain all shape information. Second, the inverse transform does not necessarily result in a closed contour. Furthermore, as Richard and Hemami have pointed out [38], this type of FD is very sensitive to the noisy fluctuations inherent in a fuzzy boundary.

The approach taken in this work is based on a complex-valued contour description and essentially the discrete version of the FD suggested by Granlund [35] and later refined by Persoon and Fu [39]. The contour is traced, thereby yielding a complex, periodic function of time. The FD expansion of this function retains all shape information.

Two contours are analyzed and compared by means of their FD parameters. Minimization of the Euclidean norm of the FD parameters of two contours results in estimates for lateral displacement, rotation and scaling that match the contours in the optimum sense. In many cases of application, the contours are sufficiently smooth such that the FS converges rapidly. In those instances, the matching procedure can be undertaken with few low-order coefficients only.

The inverse transformation of a truncated FD leads to closed contours that are a smoothed least-squares approximation of the original contour. It will be shown that the inverse transformation of the two lowest-order coefficients results in an ellipse fitting the original contour in the least-squares sense.

It should be noted that the FD is a method to describe and analyze general, closed contours and therefore can be applied not only for gray-level contours of satellite images, but also for isobars and other lines connecting points of equal value of a physical parameter.

5.2 Theory of the Complex Fourier Descriptor

5.2.1 Definition

We are given a continuous, closed contour C in the continuous x-y-plane. By tracing this contour with constant velocity, a complex, periodic time function

$$z(t) = x(t) + j\, y(t) \tag{68}$$

is defined for all contour points. The velocity of traversing the contour is chosen such that the time required to complete one period is $T = 2\pi$, with arbitrary starting point. Hence the fundamental angular frequency of $z(t)$ is equal to 1.

The Fourier descriptor (FD) of C then is defined as the complex Fourier series expansion of $z(t)$, i.e.,

$$z(t) = \sum_{n=-\infty}^{\infty} c(n)\, \exp(jnt) \tag{69}$$

where the complex coefficients $c(n)$ are given by

$$c(n) = \frac{1}{T} \int_{-T/2}^{T/2} z(t)\, \exp(-jnt)\, dt. \tag{70}$$

The coefficients $c(n)$ can be expressed in terms of their real and imaginary part as

$$c(n) = a(n) + j\, b(n) \tag{71}$$

or in terms of amplitude and phase as

$$c(n) = \rho(n)\, \exp(j\phi(n)). \tag{72}$$

The FD can be viewed as the power spectrum of the contour fluctuations. Convergence of (69) is assured at any t and uniformly on any closed interval, whenever the Dirichlet conditions are satisfied, i.e., for each finite, closed contour with a finite number of discontinuities. Smooth contours result in rapid convergence of the Fourier series coefficients $c(n)$. Since $z(t)$ is a complex function, in general $c^*(n) \neq c(-n)$, with the asterisk denoting the complex conjugate.

5.2.2 Properties of the FD

The zeroth coefficient $c(0)$ according to (70) is given by

$$c(0) = \frac{1}{T} \int_{-T/2}^{T/2} z(t) \, dt, \tag{73}$$

and therefore is equal to the complex valued location x_c, y_c of the contour's centroid, i.e.,

$$\begin{aligned} x_c &= \text{Re}\,\{c(0)\} = a(0) \\ y_c &= \text{Im}\,\{c(0)\} = b(0). \end{aligned} \tag{74}$$

The geometric operations of scaling, rotation and starting point shift are associated with simple arithmetic operations on the FD. Table 5 contains a listing of these operations in the image (time) and the frequency domain. Note that the amplitude spectrum of the FD does not change with any of the geometric operations listed in Table 5, with the exception of the zero-frequency term $c(0)$ indicating a lateral displacement of the contour.

Table 5. Geometric operations and the Fourier descriptor.

Geometric Operation	Image Domain	Frequency Domain
1) original contour	$z(t)$	$\{c(n)\}_{-\infty}^{\infty}$
2) lateral shift by x_1, y_1	$w(t) = z(t) + B$ with $B = x_1 + jy_1$	$d(0) = c(0) + B$ $d(n) = c(n)$ for $n \neq 0$
3) rotation around centroid	$w(t) = z(t) \exp(j\phi)$	$d(0) = c(0)$ $d(n) = c(n) \exp(j\phi)$ for $n \neq 0$
4) scale change	$w(t) = s\,z(t)$	$d(n) = s\,c(n)$
5) shift of starting point $0 < \alpha < 2\pi$	$w(t) = z(t - \alpha)$	$d(0) = c(0)$ $d(n) = c(n) \exp(jn\alpha)$ for $n \neq 0$

A shift of the starting point along the contour results in a phase shift, as it is well known from the Fourier theory of real, periodic functions.

The area enclosed by its FD can be given in terms of the coefficients $c(n)$ as [39]

$$S = - \sum_{n=-\infty}^{\infty} |c(n)|^2 \, n\pi. \tag{75}$$

5.2.3 Matching Contours by Means of the FD

The match of two contours C and D with their respective complex functions $z(t)$ and $w(t)$ can be expressed by means of their FD series $\{c(n)\}$ and $\{d(n)\}$. As a measure of closeness between these two FD series we choose the Euclidean norm

$$d(C,D) = \left\{ \sum_{n=-\infty}^{\infty} |c(n) - d(n)|^2 \right\}^{\frac{1}{2}}. \tag{76}$$

According to Parseval's theorem,

$$d^2(C,D) = \int_0^T |z(t) - w(t)|^2 dt, \tag{77}$$

i.e., minimization of the Euclidean norm corresponds to the minimization of the mean-square difference of the two contours $z(t)$ and $w(t)$.

Another important result of the theory of Fourier series states, when applied to contour functions, is that the contour obtained from a truncated Fourier series, i.e., the function

$$z_{-M,M}(t) = \sum_{n=-M}^{M} c(n) \exp(jnt), \tag{78}$$

approximates the original contour $z(t)$ in the least squares sense. With this result in mind, minimization of the Euclidean norm can be performed on the truncated FD series with the finite sum

$$d(C,D) = \left\{ \sum_{n=-M}^{M} |c(n) - d(n)|^2 \right\}^{\frac{1}{2}} \tag{79}$$

Since our interest is directed towards estimation of rotation β, scale factor s and starting point shift α that would map a contour z(t) into a second contour w(t) while obtaining a minimum Euclidean norm, the sum

$$J(C,D) = \sum_{\substack{n=-M \\ n \neq 0}}^{M} |c(n) - s\, d(n) \exp(j(\beta + n\alpha))|^2 \tag{80}$$

has to be minimized with respect to the parameters s, β, and α. The coefficients c(n) and d(n) of (80) are the FD of the contours z(t) and w(t), respectively. Note that the zero-order coefficients c(0) and d(0) are not included in (80) since they indicate the lateral shift of the centroid.

The following is a brief summary of Persoon and Fu's scheme to solve this minimization problem [39]. Suboptimal procedures were suggested in the same paper [39] and by Wallace and Mitchell [40], but are not considered at this point.

Set $c^*(n)\, d(n) = \sigma(n) \exp(j\psi(n))$. Minimization of (80) then is equivalent to minimizing

$$J(C,D) = \Sigma c(n)\, c^*(n) + s^2\, \Sigma\, d(n)\, d^*(n)$$

$$- 2\, s\, \Sigma\, \sigma(n) \cos(\psi(n) + n\alpha + \beta).$$

The summation Σ is taken over the indices from -M to M, $n \neq 0$. The partial derivatives of this expression with respect to s, β, and α then are set to zero, and we obtain

$$s = \frac{\Sigma\, \sigma(n)\, \cos(\psi(n) + n\alpha + \beta)}{\Sigma\, d(n)\, d^*(n)}, \tag{81}$$

$$\tan\beta = -\frac{\Sigma\sigma(n) \ \sin(\psi(n) + n\alpha)}{\Sigma\sigma(n) \ \cos(\psi(n) + n\alpha)} \qquad (82)$$

and

$$\tan\beta = -\frac{\Sigma\sigma(n) \ n \ \sin(\psi(n) + n\alpha)}{\Sigma\sigma(n) \ n \ \cos(\psi(n) + n\alpha)} \ . \qquad (83)$$

By combining (82) with (83) we obtain an equation in α

$$f(\alpha) = \Sigma\sigma(n) \ \sin(\psi(n) + n\alpha) \ \Sigma \ n\sigma(n) \ \cos(\psi(n) + n\alpha)$$

$$- \ \Sigma\sigma(n) \ \cos(\psi(n) + n\alpha) \ \Sigma \ n\sigma(n) \ \sin(\psi(n) + n\alpha). \qquad (84)$$

In order to determine the optimum values $\hat{s}$, $\hat{\beta}$ and $\hat{\alpha}$, we first solve $f(\alpha) = 0$. Note that $f(\alpha)$ is a periodic function with several roots $f(\alpha_i) = 0$. For each possible shift of starting point α_i, the angle of rotation β and the scale factor s are calculated according to (82) or (83), and (81), and the Euclidean norm (80) evaluated. The set of β, α, and s is optimum when the absolute minimum of (80) is achieved.

Since (84) cannot be solved analytically, a numerical root finding algorithm has to be employed. Since the FD of smooth contours converge rapidly, the summation in (81) to (84) is performed in those cases only over a small number of terms.

5.2.4 Discrete Fourier Descriptor and Aliasing Effects

In all practical cases of application, a contour is given as a sequence of discrete points in the x-y plane. It is therefore of interest to study the relationship between the continuous and discrete Fourier descriptors.

Assume that we are given N points of a continuous contour $z(t)$. These points should be spaced such that the time interval between two points is $2\pi/N$. With (69) the FD for this discretized contour then is

$$z(k\frac{2\pi}{N}) = \sum_{n=-\infty}^{\infty} c(n) \ \exp(jnk\frac{2\pi}{N}), \ k=0, \ 1, \ . \ . \ . \ N-1. \qquad (85)$$

Since the index of the summation, n, can be written modulo N, i.e.,

$$n = m + rN, \qquad \text{with } m=0,1 \ldots N-1$$
$$r \text{ any integer,} \tag{86}$$

the exponential term of the right-hand side of (85) can be re-written

as

$$\exp(jnk2\pi/N) = \exp(j(m+rN)k2\pi/N) = \exp(jmk2\pi/N),$$

and Eq. (85) becomes

$$z(k2\pi/N) = \sum_{m=0}^{N-1} \sum_{r=-\infty}^{\infty} c(m+rN) \exp(jk(m+rN)2\pi/N)$$

or

$$z(k) = \sum_{m=0}^{N-1} \exp(jmk2\pi/N) \, \tilde{c}(m), \qquad k=0,1, \ldots N-1 \tag{87}$$

with the aliased coefficient

$$\tilde{c}(m) = \sum_{r=-\infty}^{\infty} c(m+rN). \tag{88}$$

Also note that

$$\tilde{c}(-m) = \tilde{c}(N-m). \tag{89}$$

Equation (87) is the discrete Fourier descriptor, based on a finite

sum of the aliased FD coefficients $\tilde{c}(m)$. Note that, in general, the

original coefficients $c(n)$ and the aliased coefficients $\tilde{c}(n)$ are not

identical. However, if $z(t)$ is trigonometric, i.e.,

$$z(t) = \sum_{n=-M}^{M} c(n) \exp(jnt),$$

and if $N > 2M + 1$, then

$$c(n) = \tilde{c}(n) \text{ for } |n| \le M$$

$$c(n) = 0 \quad \text{for } |n| > M.$$

The aliased, discrete FD coefficients can be obtained from the discrete

contour points $\{z(k)\}_0^{N-1}$ as follows. For the finite number of contour

points, the integral (70) becomes

$$g(n) = \frac{1}{N} \sum_{m=0}^{N-1} z(m2\pi/N) \exp(-jnm2\pi/N). \tag{90}$$

Now, (87) is inserted into (90) yielding

$$g(n) = \frac{1}{N} \sum_{m=0}^{N-1} \sum_{k=0}^{N-1} \tilde{c}(k) \exp(jkm2\pi/N) \exp(-jmn2\pi/N)$$

$$= \frac{1}{N} \sum_{k=0}^{N-1} \tilde{c}(k) \sum_{m=0}^{N-1} \exp(jm(k-n)2\pi/N). \tag{91}$$

The right summation of (91) can be written as

$$\frac{\exp(jN(k-n)2\pi/N) - 1}{\exp(j(k-n)2\pi/N) - 1} = \begin{cases} 0 & \text{for } k \neq n \\ N & \text{for } k = n, \end{cases}$$

and therefore

$$g(k) = \frac{1}{N} \tilde{c}(k) \cdot N$$

The discrete FD then is given by the pair of equations

$$\tilde{c}(k) = \frac{1}{N} \sum_{m=0}^{N-1} z(m) \exp(-jkm2\pi/N) \tag{92a}$$

$$z(k) = \sum_{m=0}^{N-1} \tilde{c}(m) \exp(jmk2\pi/N) \tag{92b}$$

5.2.5 Truncation of the Discrete FD

The objective of this section is to show that the inverse transform of a truncated FD is a least squares approximation of the original discrete contour, i.e., that

$$z^{\hat{}}(k) = \sum_{m=-M}^{M} \tilde{c}(m) \exp(jmk2\pi/N), \text{ for } 2M + 1 < N \tag{93}$$

is a least-squares approximation to (92b), i.e.,

$$J = \sum_{k=0}^{N-1} |z(k) - z'(k)|^2 \tag{94}$$

is minimum for $z'(k)$ as given by (93).

Assume, $z'(k)$ is not given by (93), but by the FD sequence $\{d(k)\}$, i.e.,

$$z'(k) = \sum_{m=-M}^{M} d(k) \exp(jmk2\pi/N),$$

or, in terms of real and imaginary parts, by

$$z'(k) = \sum_{m=-M}^{M} \exp(jmk2\pi/N) \cdot (a(m) + jb(m)).$$

With $z(k) = x(k) + jy(k)$, the function

$$J(x,y,a,b) = \sum_{k=0}^{N-1} \left\{ \left[x(k) - \sum_{m=-M}^{M} (a(m) \cos(\tfrac{2\pi}{N}mk) - b(m) \sin(\tfrac{2\pi}{N}mk)) \right]^2 \right.$$

$$\left. + \left[y(k) - \sum_{m=-M}^{M} (a(m) \sin(\tfrac{2\pi}{N}mk) + b(m) \cos(\tfrac{2\pi}{N}mk)) \right]^2 \right\}$$

is to be minimized with respect to all $a(k)$, $b(k)$. Setting the partial derivatives of $J(x,y,a,b)$ with respect to $a(k)$ equal to zero, one obtains after some lengthy algebraic operations

$$\sum_{k=0}^{N-1} \sum_{m=-M}^{M} a(m) \left[\cos(\tfrac{2\pi}{N}mk) \cos(\tfrac{2\pi}{N}nk) + \sin(\tfrac{2\pi}{N}mk) \sin(\tfrac{2\pi}{N}nk) \right] =$$

$$\sum_{k=0}^{N-1} x(k) \cos(\tfrac{2\pi}{N}nk) + y(k) \sin(\tfrac{2\pi}{N}nk) \tag{95}$$

Note that the right-hand side of (95) is equal to $N \tilde{a}(n)$, with $\tilde{a}(n)$ the real part of the aliased coefficient $\tilde{c}(n)$. Hence

$$\frac{1}{N} \sum_{m=-M}^{M} a(m) \sum_{k=0}^{N-1} \cos(\tfrac{2\pi}{N}k(m-n)) = \tilde{a}(n). \tag{96}$$

Since the second summation in (96) is equal to N for m = n, but 0 otherwise, it follows that

a(n) = ã(n)   for -M $\leq$ n $\leq$ M.

A similar result can be obtained for b(n), namely, b(n) = b̃(n) for -M$\leq$n$\leq$M. We therefore conclude that the 2M+1 nonzero coefficients d(n), -M$\leq$n$\leq$M, of a discrete contour with N points, N>2M+1, that approximates the original contour of N points and N FD coefficients in the least-squares sense, are identical to the 2M+1 low-order FD coefficients c̃(n) of the original contour, i.e.,

d(n) = c̃(n) for -M$\leq$n$\leq$M.

5.2.6 Elliptic Approximation of Closed Contours

We are given a discrete, closed contour $\{z(k)\}_0^{N-1}$ with FD coefficients $\{c(n)\}_0^{N-1}$. Assume that the FD coefficients are truncated such that

$$\{d(n)\}_0^{N-1} = \begin{cases} c(n) & \text{for } n = 0 \\ 0 & \text{otherwise.} \end{cases} \tag{97}$$

The FD series expansion on {d(n)} then equals

y(k) = c(0),

i.e., the contour has degenerated to a single point, namely, the centroid of the original contour. As we have seen before, the zero-order coefficient indicates lateral displacement of the contour, if it is evaluated for two consecutive cloud images.

Now assume that the truncation is performed on two coefficients, i.e.,

$$\{d(n)\}_0^{N-1} = \begin{cases} c(n) & \text{for } n=0,1. \\ 0 & \text{otherwise.} \end{cases} \tag{98}$$

The expansion on these coefficients then equals

$$y(k) = c(0) + c(1) \exp(jk\frac{2\pi}{N}),$$

i.e., a circle centered at $c(0)$ and with radius $|c(1)|$. From the results of the foregoing section it is apparent that this circle is a least-squares approximation to the original contour $z(k)$. Since rotation and starting point are irrelevant for the description of a circle, the first two FD coefficients could be employed to estimate lateral displacement and scale changes between two contours. Note that $y(k)$ results in a closed figure with equidistant contour points.

The truncation according to

$$\{d(n)\}_0^{N-1} = \begin{cases} c(n) & \text{for } n=0,1,N-1; \text{ i.e., for } n=-1,0,1 \\ 0 & \text{otherwise} \end{cases} \tag{99}$$

leads to a curve

$$y(k) = c(0) + c(1) \exp(jk\frac{2\pi}{N}) + c(-1) \exp(-jk\frac{2\pi}{N}). \tag{100}$$

For $k=0,1,\ldots N-1$, (100) is identical to the equation of N points lying on a general ellipse in the complex plane, centered at $c(0)$. The parameters of this ellipse, i.e., major and minor axis and angle of inclination, are not as readily available as for the circle. The equation of the general ellipse in parameter form, centered at the origin, is given by

$$z(s) = \frac{a+b}{2} \exp(j\theta) \exp(j(s-s_0)) + \frac{a-b}{2} \exp(j\theta) \exp(-j(s+s_0)) \tag{101}$$

with s the parameter $0 \leq s \leq 2\pi$, a the length of the major axis, b the length of the minor axis, θ the angle of inclination, and s_0 the shift of the starting point, $0 \leq s_0 \leq 2\pi$.

The parameters of the ellipse are therefore determined from the FD coefficients by the following equations:

$$|c(1)| = \frac{a+b}{2}$$

$$|c(-1)| = \frac{a-b}{2}$$

$$\arg[c(1)] = \theta + k_0$$

$$\arg[c(-1)] = \theta - k_0 \tag{102}$$

with k_0 the integral shift of the starting point. It appears that the elliptic approximation by truncation of the FD can be used to estimate lateral displacement, rotation, scale change and shift of starting point of two consecutive contours. One should keep in mind, however, that these estimates are based on a very smooth approximation of the contour, and that, in general, better estimates are obtained with a higher-order truncation and the minimization of the Euclidean norm as discussed in Section 5.2.3. Nevertheless the elliptic approximation delivers estimates very fast and might be satisfactory in situations where the original contour has assumed a somewhat elliptic shape.

Note that the points described by Eq. (100) are points of a continuous ellipse, but that these points are not equidistantly spaced. In other words, the FD of a discretized ellipse does not result in only three non-zero coefficients $c(0)$, $c(-1)$ and $c(1)$. The parameter s in (101) is not the pathlength. Pathlength $p(s)$ as a function of this parameter s is given by the elliptic integral of the second kind

$$p(s) = a \int_0^s \sqrt{1 - \frac{a^2 - b^2}{a^2} \sin^2\psi} \, d\psi. \tag{103}$$

The total circumference $p(s=2\pi) = A$ corresponds to $t = 2\pi$ seconds tracing time. Tracing time t and completed pathlength are therefore related by

$$t(s) = \frac{2\pi}{A} p(s),$$

with s the parameter of the ellipse (101). The inverse transform of
a truncated FD (99) therefore does not result in an ellipse, but in a
set of points being a subset of the ellipse. The effect that these
points are not equidistantly spaced along the continuous elliptic curve,
could be viewed as the Gibb's phenomenon of the Fourier descriptor.

5.3 Results

The FD was introduced so far for closed contours in the complex
x-y-plane (see (68)). Since our images are defined along an n,m matrix
scheme, the notation requires a slight modification. From now on we
shall define, without loss of generality, a contour as a sequence of
points in the continuous $\tilde{n},\tilde{m}$ plane as

$$z(k) = \tilde{m}(k) + j\tilde{n}(k), \quad k = 0,1,\ldots N-1. \tag{104}$$

This $\tilde{n},\tilde{m}$ plane is identical to the one defined in Chapter 4. The
image pixels are located on its integral grid points.

The extraction of contours is usually perceived as a form of
edge detection and often based on statistic assumptions of image and
image noise [42,43]. Since our contours are defined as lines of con-
stant gray level, they do not necessarily coincide with physical edges.
Also most of the contour followers found in the literature do not
always guarantee the generation of a closed contour. Because the
images on hand are usually received with a very high signal-to-noise
ration, image noise is not a problem.

Therefore a very simple gradient technique was chosen that had
been applied successfully to radar echos [44]. With this method all
points of the $\tilde{n},\tilde{m}$ plane are identified where the specified threshold

level is intersected by the linear interpolation of two neighboring pixels.

The whole contour analysis program runs interactively. The cloud analyst selects features of interest from a displayed cloud image and determines the threshold along which a contour is to be drawn, by either interpreting a histogram, or, as in the case of IR imagery, by his interest in a particular temperature level.

The cursor then is moved into the area which is expected to be the inside of the cloud contour, and the contour search initiated.

At first the starting point of the contour has to be found. The search is started at the position of the cursor and extended towards the positive m (horizontal) direction, until a pixel value is found that is lower than the given threshold. The location of the first contour point then is determined by a linear interpolation between the pixel values inside and outside the contour, and its intersection with the threshold plane. The search for further points then is continued as follows. Each point of intersection leads the contour either into the inside of a 2 x 2 pixel square, or out of it (see Fig. 8).
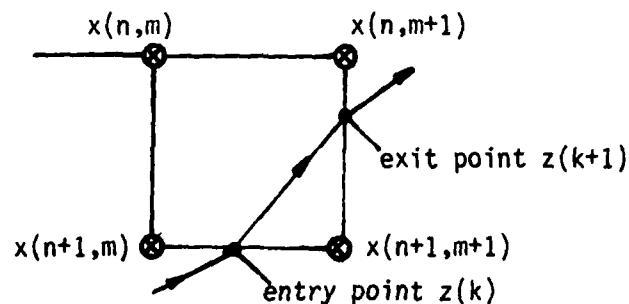
Figure 8. 2 x 2 pixel square and contour points of entry and exit.

If an entry point is found, a search for the exit point is performed counter-clockwise along the border lines of that square. The

exit point determines a new entry point for the neighboring square, and so the search is continued.

The algorithm works very fast (ca. 10 seconds for a contour of 2000 points), and the generated contour is displayed as an overlay on top of the cloud image. If the operator chooses to select this contour, all points are stored in a file. Otherwise the operator can move the cursor to a different location and/or select a different threshold in order to generate a different contour.

Storage of the contour points is performed in form of the $\tilde{n},\tilde{m}$-floating point values of the coordinates. Another possibility is to convert the real coordinates to the nearest-neighbor integers and store the contour by its chain-code [45]. In any case, the contour has to be re-sampled to obtain real-valued contour points in the $\tilde{n},\tilde{m}$ plane such that their spacing is constant. Note that if two contours are to be compared with each other, they must have the same number of contour points, evenly spaced along the contour. That coincides with the requirement of tracing the contours with a constant speed such that each circumference is done in 2π seconds.

The process of re-sampling therefore starts with the determination of the total circumference and the spacing period. For sake of simplicity, the circumference was evaluated along the piecewise linear contour given by the entry and exit points. The location of the equidistantly spaced new contour points, however, was calculated by a two-dimensional quadratic interpolation scheme. Performance tests with simple geometric figures showed that the amount of noise that was generated, had hardly any impact on the motion analysis. The advantage of this re-sampling scheme consists of the computation speed that is achieved.

Figure 9 shows a typical result of a piecewise linear cloud
contour and the re-sampled contour points. The Fourier descriptor then
is obtained by a Fast Fourier Transform (FFT) technique. Figure 10
depicts the amplitude spectrum of the FD as obtained from the contour
of Fig. 9.
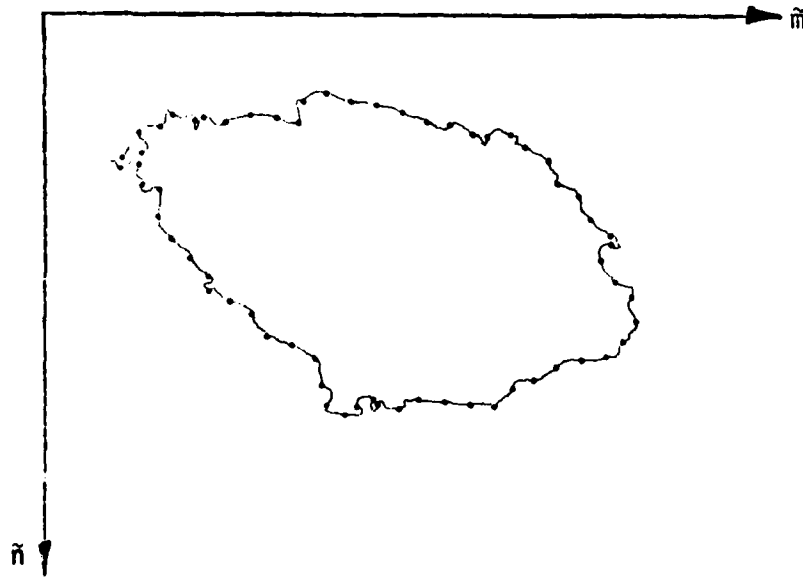
Figure 9. Example of piece-wise linear cloud contour and re-sampled
version (depicted as single points).

Figure 10 demonstrates the rapid convergence of the FD coeffi-
cients. It also becomes apparent that the amplitude spectrum of the FD
is not symmetric, since the contour function is complex-valued. The
process of truncation essentially sets the coefficients around $N/2$ to
zero, with N the total number of contour points. The inverse transform
of a truncated FD series generates a smoothed version of the original
contour. This effect is shown in Fig. 11 for the truncation of the FD
of contour Fig. 9. In the first case, only the coefficients $c(0)$,
$c(1)$ and $c(-1) = c(63)$ were not set to zero. The resulting curve is an
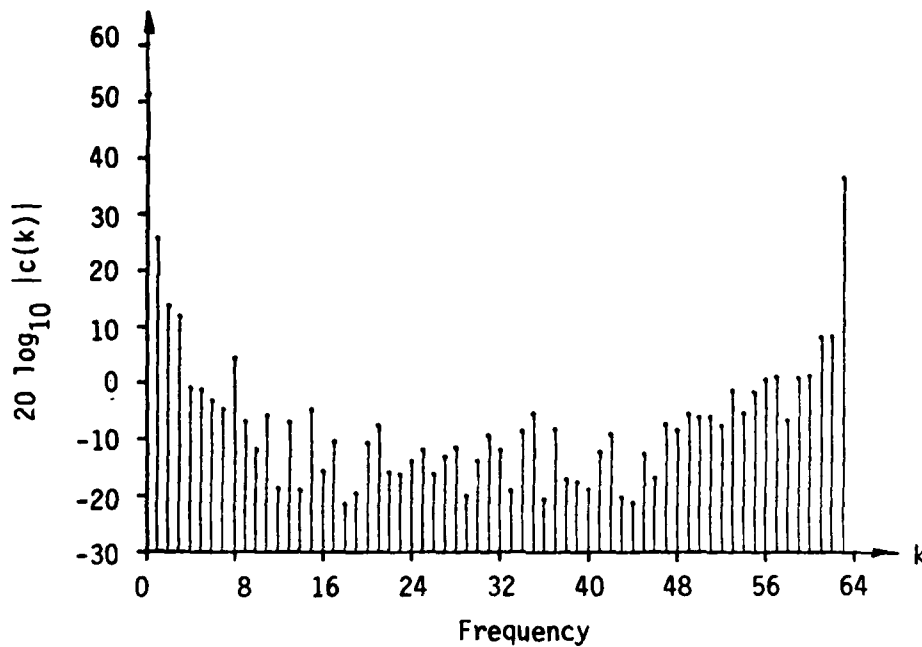
Figure 10. Absolute value of the FD coefficients obtained from the contour of Fig. 9. N = 64.

ellipse. In the second case, also the coefficients c(2) and c(-2) = c(62) were utilized. This should demonstrate that few complex numbers can well describe general, smooth contours.
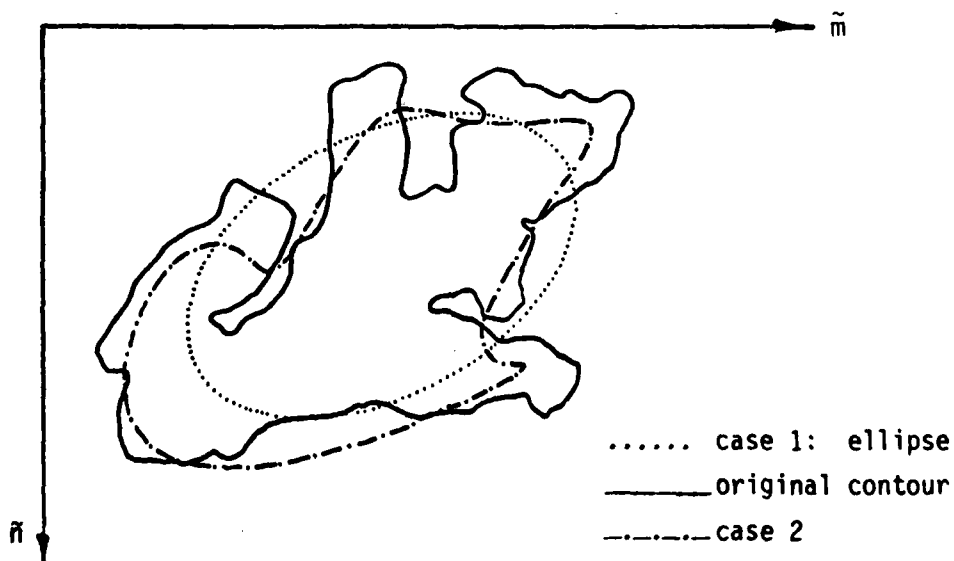
Figure 11. Inverse transform of truncated FD series; case 1: 3 non-zero coefficients, case 2: 5 non-zero coefficients.

Two contours are analyzed for lateral shift, rotation and scale changes by applying the optimization technique described in Section 5.2.3. The FD series of both contours are calculated and the order of the coefficients selected that are to be subjected to the subsequent minimization of the Euclidean norm. The roots of Eq. (84) are obtained numerically by means of Mueller's iteration scheme of successive bisection and inverse parabolic interpolation. This scheme was made self-adaptive such that the restriction on the error tolerance for the output were stepwise reduced, after a certain number of iterations had not succeeded in finding any root.

The Euclidean norm was evaluated for each root. The set of parameters for rotation, scale change and starting point shift, that resulted in an absolute minimum of the norm, was returned as the final set of estimates.

Table 6 lists some results of a contour analysis of the cloud pair II of Fig. 2. Since the lateral displacement is given by the zero-order coefficient, it is the same for all three cases of truncation. Truncation was performed as follows: for case I, $c(-1)$, $c(0)$ nonzero. This is the elliptical approximation. For case II, $c(-3)$ . . . $c(3)$ non-zero. For case III, $c(-10)$ . . . $c(10)$ nonzero. Since cloud pair II of Fig. 2 consists of well-separated clouds, the threshold level for the contour was set slightly higher than the background.

Table 6. Numerical results of the FD motion analysis of cloud pair II, Fig. 2.

Geometric Operation	Type of Truncation		
	I	II	III
Lateral Displacement, $\Delta \tilde{n}$, $\Delta \tilde{m}$	-2.2 1.6	-2.2 1.6	-2.2 1.6
Rotation in Degree	-2.6	-1.2	-0.9
Scale Change	1.1	0.9	0.9

Table 6 illustrates that the results of truncation type II and III are not dramatically different for sufficiently smooth contours. The whole analysis was performed with the PDP 11/60 equipment described earlier in this work. Computation time never exceeded 15 seconds including I/O-operations, for one pair of contours.

5.4 Summary

The method of motion analysis presented in this chapter is based on the information contained in closed contours. These contours can be defined either as encompassing a whole cloud or by following a selected level of pixel value. The contour is traced with constant velocity. The coordinate values at equidistant points along this contour are combined to a complex number. The contour therefore has become a periodic, discrete time function in the complex plane.

The Fourier descriptor (FD) is defined as the discrete Fourier series representation of the contour. Lateral displacement, rotation and scale change are simple operations in the time and frequency domain.

Smooth contours result in FD's that converge to zero rapidly. That means that few low-order FD coefficients contain most of the shape information of the contour.

Two contours can be compared by minimizing the Euclidean norm of two truncated FD series. This results in estimates for translation, rotation and scaling that would map one contour into the other. The inverse of a truncated FD series approximates the original contour in the least-squares sense. For the case of preserving only the two lowest non-zero order coefficients, the resulting contour consists of points on an ellipse. These points, however, are not any more evenly

spaced. An interactive computer program was developed that obtains the estimates of motion parameters for two consecutive contours in less than 15 seconds.

CHAPTER 6

TIME SERIES ANALYSIS AND ADAPTIVE FILTERING

6.1 Introduction

In the foregoing chapters attempts were made to define and extract parameters of motion from a given pair of cloud images. These parameters are related to lateral translation, rotation and size change.

This chapter now deals with the time series analysis of the parameters obtained from a sequence of consecutive cloud images. It is hoped that the parameter estimates obtained from past observations can be fitted to a mathematical model, upon which the prediction of future cloud motion and related weather conditions could be based. The search for such a model, or, more precisely, a class of models, is currently considered to be one of the most urgent research topics in the atmospheric sciences.

Within the framework of this research no attempt is being made to discuss the vast amount of models that have been developed for more or less general atmospheric conditions and processes.

Most of these models are based on the observation and measurement of variables and parameters that describe the physics of the atmosphere: air pressure, temperature, radiation, wind vectors, etc.

As an alternative approach to those very often complex models, this chapter is concerned only with the results of motion analysis

techniques as described in the previous parts of this work. It is assumed that besides those motion estimates no further information is available.

The problem therefore consists of the following tasks:

1. select one or more targets in the cloud scene,

2. select the technique of motion parameter estimation,

3. obtain estimates of these parameters from past satellite observations,

4. identify a model that fits these estimates according to some criterion of optimality,

5. predict future values of these parameters on the basis of the model and past observations, and

6. if desirable, update your model.

6.2 Polynomial Motion Models

Assume a point target is moving in the x-y plane. Its position x and y at times t is denoted by $x(t)$ and $y(t)$.

Assume furthermore that $x(t)$ and $y(t)$ can be modeled by polynomials in t of order m, and additive noise, i.e.,

$$x(t) = x_0 + x_1 t + x_2 t^2 + \ldots + x_m t^m + v_x(t) \qquad (105\ a)$$

$$y(t) = y_0 + y_1 t + y_2 t^2 + \ldots + y_m t^m + v_y(t) \qquad (105\ b)$$

with $x_0, \ldots, x_m, y_0, \ldots, y_m$ the coefficients and $v_x(t)$, $v_y(t)$ the noise processes. Equation (105 a) and (105 b) may be combined to the vector equation

$$\underline{z}(t) = H(t)\ \underline{c} + \underline{v}(t), \qquad (106)$$

with

$$\underline{z}(t) = \begin{pmatrix} x(t) \\ y(t) \end{pmatrix} \quad \text{the observation vector,}$$

$$H(t) = \begin{pmatrix} 1 & t & t^2 & \cdots & t^m & \vline & & & 0 & \\ \hline & & 0 & & & \vline & 1 & t & t^2 & \cdots & t^{\overline{m}} \end{pmatrix} \quad \text{the matrix}$$

of exponentials, and

$$\underline{c} = (x_0 \cdots x_m \mid y_0 \cdots y_m)^T \quad \text{the vector of}$$

unknown parameters.

An estimate of the unknown, $\hat{\underline{c}}$, can be found by the least squares technique. This method essentially produces an optimal fit of a chosen functional form (in this case a polynomial) to a given set of measurements. With m measurements $x(t_i)$, $y(t_i)$, $i = 1, \ldots, m$, we construct the vector equation

$$\underline{\tilde{z}} = \tilde{H}\,\underline{c} + \underline{\tilde{v}},$$

or, in long hand,

$$\begin{pmatrix} \underline{z}(t_1) \\ \underline{z}(t_2) \\ \cdot \\ \cdot \\ \cdot \\ \cdot \\ \underline{z}(t_m) \end{pmatrix} = \begin{pmatrix} H(t_1) \\ H(t_2) \\ \cdot \\ \cdot \\ \cdot \\ \cdot \\ H(t_m) \end{pmatrix} \underline{c} + \begin{pmatrix} \underline{v}(t_1) \\ \underline{v}(t_2) \\ \cdot \\ \cdot \\ \cdot \\ \cdot \\ \underline{v}(t_m) \end{pmatrix}. \quad (107)$$

The least-squares estimate then is obtained by solving [46]

$$\hat{\underline{c}} = (\tilde{H}^T \tilde{H})^{-1} \tilde{H}^T \underline{\tilde{z}}. \quad (108)$$

Note that for the evaluation of the estimate, all measurements have to be utilized together at one time. The matrix $(\tilde{H}^T \tilde{H})^{-1}$, also called the pseudo-inverse of $\tilde{H}$, is different for each number of measurements,

but it can be calculated before any of the observation are obtained. As with most other curve-fitting techniques, the least-squares method does not allow any insight into the underlying physical nature of the motion process. Such an attempt is made in the following section.

6.3 Dynamical Motion Systems and Recursive Filtering

Less than by a static description of the output trajectory, many physical motion processes are described rather by linear, dynamic equations.

A linear, stationary dynamic system is given in state space notation by the following vector equation:

$$\dot{\underline{x}}(t) = A \underline{x}(t) + B \underline{u}(t) \tag{109}$$

and

$$\underline{z}(t) = H \underline{x}(t) + \underline{v}(t), \tag{110}$$

where

$\underline{x}$ the $n \times 1$ state vector

$\underline{u}$ the $m \times 1$ vector of forcing functions, or noise

$\underline{z}$ the $p \times 1$ vector of observations

$\underline{v}$ the $p \times 1$ vector of measurement noise

A, B, H coefficient matrices.

Example.

Consider the mechanical system shown in Fig. 12. Let c be the spring constant and k the damping coefficient between the mass m and the floor. Newton's law, $m\, a = F$, gives

$$m\, \ddot{y}(t) = - k\, \dot{y}(t) - c\, y + u,$$

with u the external force (input).

Let us choose $y = x_1$ and $\dot{y} = x_2$ as state variables. The dynamical state-space description of the system then is given by

$$\begin{pmatrix} \dot{x}_1 \\ \dot{x}_2 \end{pmatrix} = \begin{pmatrix} 0 & 1 \\ -\dfrac{c}{m} & -\dfrac{k}{m} \end{pmatrix} \cdot \begin{pmatrix} x_1 \\ x_2 \end{pmatrix} + \begin{pmatrix} 0 \\ \dfrac{1}{m} \end{pmatrix} u$$

and

$$y = \begin{bmatrix} 1 & 0 \end{bmatrix} \begin{pmatrix} x_1 \\ x_2 \end{pmatrix}.$$
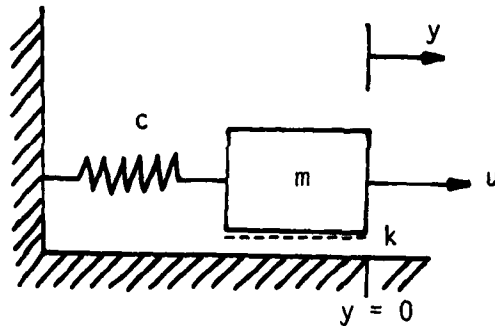
Figure 12. Example of dynamic motion process.

Discrete, dynamical systems are governed by difference equations. A stationary, linear discrete dynamical system is given in state space notation as

$$\underline{x}(k) = \Phi \, \underline{x}(k-1) + \underline{w}(k-1) \tag{111}$$

$$\underline{z}(k) = H \, \underline{x}(k) + \underline{v}(k) \tag{112}$$

with Φ the state transition matrix. If a continuous system is given, but the observations are taken in discrete time instances, the whole system can be discretized and the transition matrix Φ derived from the matrix A of Eq. (109).

The state vectors of both continuous and discrete dynamical systems can be estimated recursively by means of the Kalman filter. Since our cloud image observations are obtained at discrete times, we shall summarize the Kalman-filter equations only for the discrete case. For the system given by (111), (112), assume

$$\underline{w}(k) = N(\underline{0}, Q(k))$$

and $\quad \underline{v}(k) = N(\underline{0}, R(k)).$

With the initial estimates

$$\hat{x}(0) = E[x(0)]$$

and the error covariance

$$P(0) = E[(x(0) - \hat{x}(0))(x(0) - \hat{x}(0))^T],$$

(113)

the extrapolation or prediction of the state estimates and the error covariance matrix is performed according to

$$\hat{x}(k+1 \mid k) = \Phi\hat{x}(k)$$

(114)

and

$$M(k+1) = \Phi P(k) \Phi^T + Q(k).$$

(115)

With the new measurement $\underline{z}(k+1)$ arriving, the new state estimate is given by

$$\hat{x}(k+1) = \hat{x}(k+1 \mid k) + K(k) [z(k+1) - H \hat{x}(k+1 \mid k)],$$

(116)

with $K(k)$ the Kalman gain matrix given as

$$K(k) = M(k) H^T [H M(k) H^T + R(k)]^{-1}.$$

(117)

The error covariance is updated according to

$$P(k+1) = [I - K(k) H] M(k+1).$$

(118)

The recursion continues with Eq. (114).

The Kalman filter is the optimum linear state estimator against an expected-squared error cost function even without the assumption of Gaussian noise distribution [47].

6.4 Kalman Filter Tracking of Moving Objects

Recursive tracking algorithms based on the Kalman filter have entered the literature about 10 years ago and gained considerable attention since then. With respect to the transition matrix, the proposed models may be divided into two groups.

The first type is usually applied to the estimation of the track of non-maneuvering re-entry vehicles [48, 49]. The model used in this approach is closely based on the physical equation of motion and includes typically drag, gravity, centrifugal and Coriolis force vectors [48]. Since some of these parameters are unknown, the state vector equation becomes a non-linear estimation problem and is usually solved via an extended Kalman filter [48, 50].

It appears to be desirable, to introduce a similar approach to the motion of clouds. The horizontal equation of motion of an air parcel is given in pressure coordinates as [51]

$$\frac{d\underline{v}}{dt} = -\nabla\Phi - f\,\underline{k} \times \underline{v} - a\,\underline{v}, \tag{119}$$

with $\nabla\Phi$ the horizontal pressure gradient force, $f\,\underline{k} \times \underline{v}$ the Coriolis force, and $a\,\underline{v}$ the frictional drag; $\underline{v}$ is the velocity vector, Φ the pressure field, f the Coriolis parameter, $\underline{k}$ the unit vector in vertical direction, and a the drag coefficient.

Even if we assumed that the motion of clouds coincides with the dynamic motion of air flow, we would again obtain a non-linear estimation problem and would have to resort to an extended Kalman filter. A thorough study of the feasibility and ramification of such an approach is recommended for further research. An extended Kalman filter is likely to work satisfactorily for a very large number of observations.

However, our case studies on hand never exceeded 12 measurements of cloud displacement.

The second type of Kalman filter for tracking purposes is derived from a Taylor series representation of the transition matrix. The position $x(t=T)$ of the object can be given by the Taylor series expansion in terms of the derivatives of $x(.)$ as

$$x(T) = x(0) + T \dot{x}(0) + \frac{T^2}{2} \ddot{x}(0) + \frac{T^3}{6} \dddot{x}(0) + \ldots \text{HOT}, \qquad (120)$$

with HOT denoting the higher order terms. The series expansion (120) exists for continuous trajectories $x(t)$.

Assume for example that the motion process can be modeled in such a way that the second and all higher derivatives are equal to zero, i.e.,

$$x(T) = x(0) + T \dot{x}(0)$$

$$y(T) = y(0) + T \dot{y}(0).$$

With T the time lapse between two observations, the displacement of the target then is governed by the state space equation

$$\underline{x}(k) = \Phi \; \underline{x}(k-1)$$

or

$$\begin{pmatrix} x \\ \dot{x} \\ y \\ \dot{y} \end{pmatrix}_k = \begin{pmatrix} 1 & T & 0 & 0 \\ 0 & 1 & 0 & 0 \\ 0 & 0 & 1 & T \\ 0 & 0 & 0 & 1 \end{pmatrix} \cdot \begin{pmatrix} x \\ \dot{x} \\ y \\ \dot{y} \end{pmatrix}_{k-1} \cdot$$

If there remains some doubt about the truncation of Taylor series, the residual can be treated as an additional noise term [52 - 56]. If it is assumed that the target has the ability to maneuver, this residual noise term might become highly correlated. In these cases an augmented

state vector is formed with the correlation coefficient as additional element in the transition matrix [52, 54].

Common to all Kalman filter tracking techniques are the following disadvantages:

1. If the noise covariance matrices $Q(k)$ and $R(k)$ are not exactly known, the filter becomes sub-optimal.

2. Even if the initial state estimates are well placed, the recursion needs, depending on the complexity of the system and the signal-to-noise ratio, a relatively large number of observations in order to converge. In the case of radar target tracking, several hundred measurements are required to identify the object's path. The more maneuvering capability the object possesses, the complexer the tracking system has to be designed, and measurements are required at an even higher rate.

6.5 Results

At the beginning of the research it was hoped that cloud motion could be modeled with respect to lateral translation, rotation and scaling. Sequences of images were obtained depicting a variety of weather situations. Since it was anticipated that only an extended series of observations could produce motion forecasts within some confidence range, only hourly IR images were chosen, since they are received throughout the night.

As method of parameter extraction we chose the contour analysis technique by employing the Fourier descriptor. Target scenes were selected and their contour changes analyzed by a computer program

throughout the sequence of images. The derived motion parameters were listed on the line printer in form of time series data.

Several factors might have influenced the mostly unsatisfactory outcome of these studies. At first, many times a single cloud could be picked up only for 3 to 4 consecutive images. At the end of this relatively short life span, the cloud had merged or dissipated. Sometimes the identity of a cloud with respect to earlier images was unclear.

When a contour was selected along a certain temperature level, the fluctuation of the shape was often considerable. This effect may be due to the unfavorable complexity of cloud dynamics in the cases under study, and/or to diurnal changes of temperature.

One of the advantages of the FD method is the possibility to generate a future contour synthetically from the present contour and predictions of rotation, lateral displacement and scaling. However, in almost none of the cases a confident prediction could be made.

The best results were achieved in those few instances, when the motion of the selected features was less chaotic, i.e., when the features propagated in a relatively smooth path and participated all in a large system of air flow. In those cases the parameters of interest could be picked up for one cloud feature, and as soon as this feature had become inconsistent, a new feature was searched for, in the hope to obtain an uninterrupted motion analysis for the governing atmospheric system.

It has become apparent that more research has to be undertaken in order to demonstrate the feasibility of the motion analysis and prediction, as it was intended for this work.

One of the future objectives will be to obtain more frequent observations. It is true though that the cases considered for this work depicted only severe weather situations with admittedly high complexity.

The following figures and tables are to illustrate the problems that were encountered. The imagery covers the southern parts of the U.S. and the Gulf of Mexico, and consists of 18 IR images taken on Nov. 20, 1979, from 18:03 on every hour, with the exception of a missing image for 01:00 Z hours. An example is given in Fig. 13.

Five target features were selected. Their contour is shown in Fig. 14. Not all features, however, could be observed at the same time. Coverage of these features and the respective temperature level is listed in Table 7.

Figure 13. First image of case study.
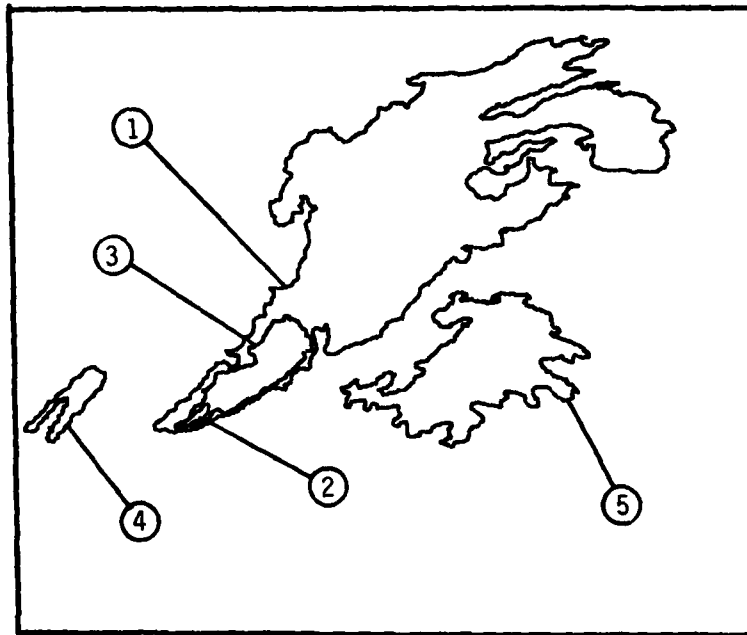
Figure 14.   Features selected for case study.

Table 7. Coverage of features and temperature level of contour.

Image received at	Features and Temperature in Celsius

18:03

19:03

20:03

21:03

22:03

23:03   -54°

00:04   -18°

01:04   no observation

02:04   -18°

03:03

04:03

05:03

06:03

07:03

08:03   -33°

09:03   -47°

The numerical results of the motion analysis are listed in Tables 8 -
12. For each listed time instance, the differences of the contour
parameters with respect to the earlier observation are entered. These
parameters are: lateral displacement, rotational and scale changes by
evaluating only 2 FD coefficients, and the same by utilizing 10 FD
coefficients.

Table 8. Motion analysis for feature No. 1.

Time	lateral displacement		2 FD Coefficients		10 FD Coefficients	
	Δñ	Δm̃	Rotation	Scale Change	Rotation	Scale Change
19:03	-2.23	11.2	-3.3	0.97	-4.31	0.96
20:03	-4.5	4.86	0.7	1.04	1.85	1.03
21:03	-1.23	6.07	-1.4	0.99	-2.35	0.97
22:03	1.85	4.01	-1.72	0.99	-1.48	0.98
23:03	-6.9	9.6	-0.25	0.97	0.47	0.97
00:04	-6.1	13.3	-5.25	1.16	-3.80	1.01
01:04	---------------------no data available---------------------					
02:03	3.6	-6.4	3.63	0.82	6.05	0.83
03:03	-6.4	5.4	2.45	1.15	1.75	1.07
04:03	0.5	-14.7	10.1	1.04	10.51	1.00
05:03	-0.1	5.8	-2.04	0.95	2.37	0.93
06:03	-2.7	12.6	1.15	1.11	-0.27	1.02
07:03						
08:03						
09:03						

Table 9. Motion analysis for feature No. 2.

Time	lateral displacement $\Delta\tilde{n}$	$\Delta\tilde{m}$	2 FD Coefficients Rotation	Scale Change	10 FD Coefficients Rotation	Scale Change
19:03	-18.9	16.7	-0.22	0.96	-0.01	0.95
20:03	19.1	-11.5	-10.16	1.7	-10.24	1.68
21:03	2.5	0.0	0.4	1.75	-0.9	1.76
22:03						
23:03						
00:04						
01:04	------------------------- no data available ----------------					
02:03						
03:03						
04:03						
05:03						
06:03						
07:03						
08:03						
09:03						

Table 10. Motion analysis for feature No. 3.

Time	lateral displacement Δñ	Δm̃	2 FD Coefficients Rotation	Scale Change	10 FD Coefficients Rotation	Scale Change
19:03						
20:03	12.9	-9.1	-2.62	1.27	-3.11	1.21
21:03	-9.2	8.8	2.58	1.00	3.56	0.94
22:03	-6.8	8.4	5.55	0.91	3.03	0.91
23:03	6.7	1.9	-6.43	1.08	-7.26	1.06
00:00	-2.7	5.4	-0.49	1.02	-0.32	0.97
01:04	-----------------------		no data available		------------------	
02:03	-0.2	4.8	-4.04	0.74	-5.17	0.73
03:03	13.7	-14.4	-0.82	1.73	-0.92	1.73
04:03	-3.0	9.3	-3.18	1.25	-3.60	1.19
05:03	-0.1	2.0	0.10	1.45	2.53	1.46
06:03	0.8	1.5	0.37	0.94	2.84	0.92
07:03	-12.7	18.8	32.81	3.03	32.64	2.97
08:03						
09:03						

END
DATE
FILMED
04-82
DTIC

III 1.0

2.8   2.5

3.2   2.2

2.0

1.1   1.8

1.25   1.4   1.6
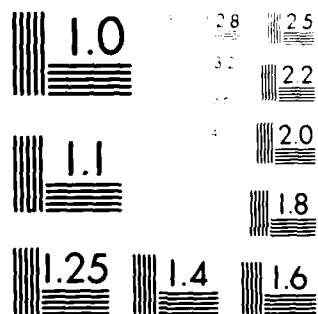
MICROCOPY RESOLUTION TEST CHART

Table 11. Motion analysis for feature No. 4.

Time	lateral displacement $\Delta\tilde{n}$	$\Delta\tilde{m}$	2 FD Coefficients Rotation	Scale Change	10 FD Coefficients Rotation	Scale Change
19:03						
20:03						
21:03						
22:03						
23:03						
00:04						
01:04	-----------------------no data available---------------------					
02:03						
03:03						
04:03	- 7.0	5.6	-11.24	0.58	-12.3	0.55
05:03	-18.9	11.9	18.36	0.69	16.6	0.67
06:03	0.5	2.83	-9.2	0.81	- 8.81	0.80
07:03	-21.3	13.2	1.27	1.50	2.45	1.46
08:03	-22.5	11.6	3.99	0.97	4.18	0.94
09:03	-12.3	6.32	-1.45	1.50	-2.16	1.48

Table 12. Motion analysis for feature No. 5.

Time	lateral displacement Δñ	Δm̃	2 FD Coefficients Rotation	Scale Change	10 FD Coefficients Rotation	Scale Change
19:03						
20:03						
21:03						
22:03						
23:03						
00:04						
01:04	------------------- no data available -------------------					
02:03						
03:03	2.1	-0.2	7.86	0.93	13.5	0.90
04:03	-0.7	15.0	0.31	0.93	-0.91	0.84
05:03	1.63	3.7	-13.34	1.03	-5.75	0.96
06:03	3.1	5.9	-1.00	0.95	-6.76	0.91
07:03	-3.7	3.5	0.88	1.02	0.53	1.01
08:03	2.85	8.6	-17.85	1.34	-17.78	1.09
09:03	-3.5	15.7	-24.28	1.56	-74.01	0.88

6.6 Summary

In this chapter we studied the problem of modelling motion processes. As long as the trajectory is considered as being a polynomial curve, the least-squares estimator can be applied. This method requires all past observations at one time. Most physical motion processes are of dynamical nature and governed by differential or difference equations. With the introduction of state-space variables, the input-output relation can be described in form of a vector equation. The model of the motion process is either derived from physical equations or from a Taylor series expansion. Estimation can be performed recursively with the Kalman filter. In the case of a physical motion system, the estimation becomes non-linear and an extended Kalman filter has to be employed. If the system is derived from the Taylor series expansion, certain assumptions are made on the maneuverability of the target. The higher order terms of the series expansion might be replaced by noise terms, but maneuver noise is usually correlated, and the state-vector has to be augmented.

Finally attempts were made to apply any of these methods to a time series of motion parameters extracted from a sequence of cloud images. These attempts were not successful since the ϵ neric processes were in all cases of a very complicated nature. Smooth trajectories existed only occasionally within a range of 3 or 4 observations. The experienced problems were discussed and recommendations for further research made.

CHAPTER 7

CONCLUSIONS

The objective of this dissertation was the analysis of cloud motion from satellite images. The problem was approached from a signal analysis point of view. Almost no consideration was given to the physical parameters and properties of the atmosphere.

Motion was defined as a change of those image parameters that describe a cloud or a cloud pattern most distinctively. The lowest level of such a descriptive signal analysis comprises lateral displacement, rotation and size changes of the cloud.

Current cloud motion analysis techniques are based on the inner product or cross-correlation method and deliver estimates only for lateral displacement. Before introducing new methods in this research that extract also rotational and size changes, an improvement of the inner product method was developed.

According to the inner product method the lateral displacement estimate is obtained by locating the maximum of the inner product surface of two consecutive images. This maximum, however, is very often not clearly identifiable, nor is this method selective with respect to any of the cloud signal features. The inner product should be evaluated only for those features that are relevant for a signal description. The separation of the clouds from the background can be considered as a fundamental selection. This dissertation shows that a considerable

90

improvement of the performance of the inner product method can be achieved by applying spatial filters to the input images prior to the inner product operation.

In order to generate sharp maximum peaks of the inner product surface, these filters are developed along some theoretical considerations as inverse filters. Since these filters possess a high-pass characteristic, the subsequently evaluated inner product is based on high-frequency image features such as boundaries, edges and texture. These features are very relevant for a description of a cloud image. The maximum inner product then indicates the energy of those high-frequency image features that have translated laterally in a homogeneous fashion. If the cloud changes are severe, this translation is not necessarily homogeneous, and the inner product might result in a multitude of relative maxima.

In these instances the filter characteristic can be changed gradually from high-pass over high-emphasis to all-pass, such that the energy of lower frequencies has more and more influence on the inner product operation.

The pre-filtering technique was tested with a variety of input images. Results were very satisfactory. The only constraint to this method (besides delivering estimates only for lateral displacement) is given by the computer power. The evaluation of the inverse filter coefficients, the filtering process and the subsequent evaluation of the inner product surface poses a serious problem to the users in a mini-computer environment.

In the following two chapters new techniques were introduced that also provide estimates on rotational and size changes. The first one

can be considered as almost the opposite to the inner product method; it is a very fast technique, identifies rotation and size changes, but is based on a very general description of the cloud signal, namely, on the fit of a normal surface to the luminance values of the image. Lines of constant density are ellipses around the center of luminance gravity. Size changes can be identified as absolute as well as by the excentricity of the ellipse. Rotation is indicated by a changing angle of inclination. This method is not necessarily very precise but can be used for a fast over-all evaluation of the cloud motion. It also can be applied to a cloud field.

The restrictions imposed on the next technique are more stringent. The meaningful cloud feature is now defined as a closed contour, be it the actual boundary of the cloud or a contour along any level of constant luminance or temperature (for IR images).

As long as the signal-to-noise ratio of the images is sufficiently high, a simple gradient technique proved to be a fast and effective contour extractor. The analysis of the contour and its changes is performed by means of the Fourier descriptor (FD). The FD is defined as the discrete Fourier series representation of the closed contour. Lateral displacement, rotation and scale change are simple operations in the space and frequency domain. Smooth contours result in FD's that converge rapidly. That means that few low-order coefficients of the FD contain most of the shape information of the contour.

Two contours are compared by minimizing the Euclidean norm of two truncated FD series. This results in estimates for translation, rotation and scaling that would map one contour into the other.

The inverse transform of a truncated FD series approximates the original contour in the least-squares sense. The inverse of the two

lowest-order FD coefficients results in an ellipse. As with the bi-variate normal fit, these ellipses can indicate lateral translation, rotation and size changes. More precise estimates are obtained from FD series that are truncated at a higher order. Assume that we are given predictions of lateral translation, rotation and size change. With the FD method then a predicted contour can be generated synthetically from the FD series of the most recent observation. Thus the cloud analyst has the option to display a predicted contour and compare later with the actual, updated observation.

An interactive computer program was developed that obtains a motion analysis from a pair of contours in less than 15 seconds with the PDP 11/60 available for this research.

In the last chapter, models for motion processes are studied. Like most other physical motion processes, cloud motion is considered to be a dynamical process that is described best in state-space notation. The model is either derived from a Taylor series expansion or from physical equations. The Taylor series approach is more general and leads to a simpler statement of the estimation problem. More research is recommended to utilize physical equations, like the horizontal equation of motion that is used to calculate wind vectors from a balance of the physical forces. Estimation of the state-space variables can be performed recursively with a Kalman filter. In the case of a model based on physical equations, the estimation problem might become non-linear, and an extended Kalman filter has to be derived. In spite of the mathematical and computational complications, such an estimator could converge faster, since it makes use of the physical properties of the atmosphere.

Several case studies of cloud image sequences were analyzed with the Fourier descriptor method. The contour parameters of various image features were extracted and listed. Attempts to find smooth trajectories succeeded only in very limited cases. Several reasons might be responsible for this failure. First, the images were given at a rate of only one image per hour. Many features therefore could be observed only over a span of 3 to 4 images. Secondly, the amount of local cloud physics and disturbances was in all cases larger than expected. Since the shape of the temperature contours of clouds is very sensitive to local effects, the author recommends to derive contours not for a particular pixel value, but for a range of values. Local effects might thereby be averaged out. It is true though that all cases considered for this work depicted severe weather situations with admittedly high complexity. Much better results are expected with a higher image rate, and more experience has to be gathered through further case studies.

REFERENCES

[1] L.F. Hubert and L.F. Whitney, Jr., "Wind estimation from geostationary-satellite pictures," Monthly Weather Review, vol. 99, No. 9, pp. 665-672, Sept. 1971.

[2] A.F. Hasler, W.E. Shenk and W.C. Skillman, "Wind estimates from cloud motions: results from phase I, II and III of in situ aircraft verification experiment," J. Appl. Meteor., vol. 16, pp. 812-815, Aug. 1977.

[3] T. Fujita, K. Watanabe and T. Izawa, "Formation and structure of equatorial anticyclones caused by large-scale cross-equatorial flows determined by ATS-I photographs," J. Appl. Meteor., vol. 8, pp. 649-667, Aug. 1969.

[4] E.A. Smith and D.R. Phillips, "Automated cloud tracking using precisely aligned ATS pictures," IEEE Trans. Comput., vol. C-21, No. 7, pp. 715-729, July 1972.

[5] J.A. Leese, C.S. Novak and V.R. Taylor, "The determination of cloud pattern motions from geosynchronous satellite image data," Pattern Recognition, Vol. 2, pp. 279-292, 1970.

[6] R.M. Endlich, D.E. Wolf, D.J. Hall and A.E. Brain, "Use of a pattern recognition technique for determining cloud motions from sequences of satellite photographs," J. Appl. Meteor., vol. 10, pp. 105-117, Feb. 1971.

[7] D.E. Wolf, D.J. Hall and R.M. Endlich, "Experiments in automatic cloud tracking using SMS-GOES data," J. Appl. Meteor., vol. 16, pp. 1219-1230, Nov. 1977.

[8] J.W. Modestino and R.W. Fries, "Construction and properties of a useful two-dimensional random field," IEEE Trans. Inform. Th., vol. IT-26, pp. 44-50, Jan. 1980.

[9] L. Fusco, R. Lunnon, B. Mason and C. Tomassini, "Operational production of sea surface temperatures from Meteosat image data," ESA Bulletin, No. 21, pp. 38-43, Feb. 1980.

[10] A.V. Oppenheim and R.W. Schafer, "Digital Signal Processing," Englewood Cliffs: Prentice-Hall, Inc., 1975.

[11] W.K. Pratt, "Digital Image Processing," New York: John Wiley & Sons, 1978.

[12] D.I. Barnea and H.F. Silverman, "A class of algorithms for fast digital image registration," IEEE Trans. Comput., vol. C-21, No. 2, pp. 179-186, Feb. 1972.

[13] J.B. Clary and R.F. Russell, "All-digital correlation for missile guidance," S.P.I.E. vol. 119: Application of Digital Image Processing, IOCC 1977, pp. 36-46, 1977.

[14] J.S. Boland, L.J. Pinson, E.G. Peters, G.R. Kane and W.W. Malcolm, "Design of a correlator for real-time video comparisons," IEEE Trans. Aerosp. Electr. Syst., vol. AES-15, No. 1, pp. 11-20, Jan. 1979.

[15] B.H. Briggs, "On the analysis of moving patterns in geophysics-- II. Dispersion analysis," J. Atmos. Terr. Phys., vol. 30, pp. 1789-1794, 1968.

[16] H. Mostafavi, "Optimal window functions for image correlation in the presence of geometric distortion," IEEE Trans. Acoust., Speech, Signal Processing, vol. ASSP-27, No. 2, pp. 163-169, April 1979.

[17] J.M. Tribolet, "A new phase unwrapping algorithm," IEEE Trans. Acoust., Speech, Signal Processing, vol. ASSP-25, No. 2, pp. 170-177, Apr. 1977.

[18] F. Bonzanigo, "An improvement of Tribolet's phase unwrapping algorithm," IEEE Trans. Acoust., Speech, Signal Processing, vol. ASSP-26, No. 1, pp. 104-105, Feb. 1978.

[19] D.E. Dudgeon, "The existence of cepstra for two-dimensional rational polynomials," IEEE Trans. Acoust., Speech, Signal Processing, vol. ASSP-23, No. 2, pp. 242-243, Apr. 1975.

[20] A. Vander Lugt, F.B. Rotz, and A. Klooster, Jr., "Character-reading by optical spatial filtering," in: Optical and Electro-Optical Information Processing, Editors: J.T. Tippett et al., pp. 125-141; Cambridge: M.I.T. Press, 1965.

[21] M.J. Lahart, "Optical area correlation with magnification and rotation," J. Opt. Soc. Am., vol. 60, No. 3, pp. 319-325, March 1970.

[22] A.D. Gara, "Real-time tracking of moving objects by optical cor-relation," Applied Optics, vol. 18, No. 2, pp. 172-174, Jan. 1979.

[23] R.M. Merserau and D.E. Dudgeon, "Two-dimensional digital filter-ing," Proc. IEEE, vol. 63, pp. 610-623, April 1975.

[24] C.H. Knapp and G.C. Carter, "The generalized correlation method for estimation of time delay," IEEE Trans. Acoust., Speech, Signal Processing, vol. ASSP-24, No. 4, pp. 320-327, Aug. 1976.

[25] J.G. Fiasconaro, "Two-dimensional nonrecursive filters," in: Picture Processing and Digital Filtering, Editor: T.S. Huang, pp. 69-129, Berlin: Springer-Verlag, 1979.

[26] S. Treitel and E.A. Robinson, "The stability of digital filters," IEEE Trans. Geosci. Electr., vol. GE-2, No. 1, pp. 6-18, Nov. 1964.

[27] J.L. Shanks, S. Treitel and J.H. Justice, "Stability and synthesis of two-dimensional recursive filters," IEEE Trans. Audio Electroacoust., vol. AU-20, pp. 115-128, June 1972.

[28] T.S. Huang, "Stability of two-dimensional recursive filters," IEEE Trans. Audio Electroacoust., vol. AU-20, pp. 158-163, June 1972.

[29] S. Treitel and E.A. Robinson, "The design of high-resolution digital filters," IEEE Trans. Geosci. Electr., vol. GE-4, No. 1, pp. 25-38, June 1966.

[30] E.L. Hall, "Computer image processing and recognition," New York: Academic Press, 1979.

[31] K.L. Peacock and S. Treitel, "Predictive deconvolution: theory and practice," Geophysics, Vol. 34, No. 2, pp. 155-169, April 1969.

[32] J. Makhoul, "Linear prediction: a tutorial review," Proc. IEEE, vol. 63, pp. 561-580, April 1975.

[33] A. Habibi, "Two-dimensional Bayesian estimate of images," Proc. IEEE, vol. 60, No. 7, pp. 878-883, July 1972.

[34] W.M. Göpfert, "Digital cross-correlation of complex exponentiated inputs," Proc. Intern. Symp. Image Processing, Interactions with Photogrammetry and Remote Sensing, Graz, Austria, pp. 63-66, Oct. 1977.

[35] G.H. Granlund, "Fourier preprocessing for hand print character recognition," IEEE Trans. Comput., vol. C-21, pp. 195-201, Feb. 1972.

[36] R.L. Cosgriff, "Identification of shape," Ohio State Univ. Res. Foundation, Columbus, Rep. 820-11, ASTIA AD 254 792, Dec. 1960.

[37] C.T. Zahn and R.Z. Roskies, "Fourier descriptors for plane closed curves," IEEE Trans. Comput., vol. C-21, No. 3, pp. 269-281, March 1972.

[38] C.W. Richard, Jr., and H. Hemami, "Identification of three-dimensional objects using Fourier descriptors of the boundary curve," IEEE Trans. Systems, Man, Cybern., vol. SMC-4, No. 4, pp. 371-378, July 1974.

[39]   E. Persoon and K.S. Fu, "Shape discrimination using Fourier descriptors," IEEE Trans. Systems, Man, Cybern., vol. SMC-7, No. 3, pp. 170-179, March 1977.

[40]   T.P. Wallace and O.R. Mitchell, "Real-time analysis of three-dimensional movement using Fourier descriptors," School of Electr. Engin., Purdue Univ., presented at the Workshop on Computer Analysis of Time-Varying Imagery, April 5-6, 1979, Philadelphia.

[41]   T. Pavlidis, "Algorithms for shape analysis of contours and waveforms," IEEE Trans. Pattern Analysis, Mach. Intellig., vol. PAMI-2, No. 4, pp. 301-312, July 1980.

[42]   N.E. Nahi and M.H. Jahanshahi, "Image boundary estimation," IEEE Trans. Comput., vol. C-26, No. 8, pp. 772-781, Aug. 1977.

[43]   H. Elliott, D.B. Cooper, F. Cohen and P. Symosek, "Implementation, interpretation and analysis of a suboptimal boundary finding algorithm," Dept. Electr. Engin., Colorado State Univers., Technical Report #JA80-DELENG-1, Jan. 1980.

[44]   S.S. Östlund, "Computer software for rainfall analyses and echo tracking of digitized radar data," NOAA Technical Memorandum ERL WMPO-15, Boulder, Colorado, March 1974.

[45]   H. Freeman, "On the encoding of arbitrary geometric configurations," IRE Trans. Electron. Comput., vol. EC-10, pp. 260-268, June 1961.

[46]   A. Gelb, Ed., "Applied Optimal Estimation," Cambridge, MA: M.I.T. Press, 1974.

[47]   J.M. Morris, "The Kalman-filter: a robust estimator for some classes of linear quadratic problems," IEEE Trans. Info. Theory, vol. IT-22, No. 5, pp. 526-534, Sept. 1976.

[48]   R.K. Mehra, "A comparison of several nonlinear filters for reentry vehicle tracking," IEEE Trans. Autom. Contr., vol. AC-16, No. 4, pp. 307-319, Aug. 1971.

[49]   C.B. Chang, R.H. Whiting and M. Athans, "On the state and parameter estimation for maneuvering re-entry vehicles," IEEE Trans. Autom. Contr., vol. AC-22, pp. 99-105, Feb. 1977.

[50]   P.S. Maybeck and D.E. Mercier, "A target tracker using spatially distributed infrared measurements," IEEE Trans. Autom. Contr., vol. AC-25, No. 2, pp. 222-225, April 1980.

[51]   J.M. Wallace and P.V. Hobbs, "Atmospheric Science--An Introductory Survey," New York: Academic Press, 1977.

[52]   R.L.T. Hampton and J.R. Cooke, "Unsupervised tracking of maneuvering vehicles," IEEE Trans. Aerosp. Electr. Syst., vol. AES-9, No. 2, pp. 197-207, March 1973.

[53] F.R. Castella and F.G. Dunnebacke, "Analytical results for the x, y Kalman tracking filter," *IEEE Trans. Aerosp. Electr. Syst.*, vol. AES-10, No. 6, pp. 891-895, Nov. 1974.

[54] J.M. Fitts, "Aided tracking as applied to high-accuracy pointing systems," *IEEE Trans. Aerosp. Electr. Syst.*, vol. AES-9, No. 3, pp. 350-368, May 1973.

[55] D.R. Morgan, "A target trajectory noise model for Kalman trackers," *IEEE Trans. Aerosp. Electr. Syst.*, vol. AES-12, No. 3, pp. 405-408, May 1976.

[56] B. Friedland, "Optimum steady-state position and velocity estimation using noisy sampled position data," *IEEE Trans. Aerosp. Electr. Syst.*, vol. AES-9, No. 6, pp. 906-911, Nov. 1973.

[57] R.A. Wiggins and E.A. Robinson, "Recursive solution to the multichannel filtering problem," *J. Geophys. Res.*, vol. 70, no. 8, pp. 1885-1891, April 1965.

APPENDIX

"PHASE UNWRAPPING IN TWO DIMENSIONS"

AI.   INTRODUCTION

In several areas of one- and two-dimensional signal processing,
the phase of the Fourier spectrum has become a subject of considerable
interest [A2]. The importance of phase in image processing was demon-
strated in recent papers [A3,A4]. The two-dimensional phase of an
image conveys usually more information to the human observer than the
amplitude. This can be explained by the relationship between phase and
the location of spectral energy within the image. The human observer
seems to gain more information from the location of spectral energy than
from its amplitude. Images obtained from the inverse transform of the
phase term only show superior resemblance to the original than those
obtained only from the magnitude. This result recently led to the
development of an image coding scheme emphasizing the phase [A4].

A numerical evaluation of the phase, however, is commonly ham-
pered by the ambiguity of the arctangent function. Phase unwrapping,
i.e., the evaluation of a continuous phase curve or phase surface, is
not only desirable to visualize phase behavior, but is also a necessary
prerequisite for the computation of the complex cepstrum if it was
chosen to follow the method of computing the complex logarithm of the
spectrum [A1,A5]. The existence of two-dimensional cepstra was shown
in [A6].

The unwrapping algorithm proposed in this correspondence is a
two-dimensional extension of Tribolet's method [A1]. It incorporates
a suggestion by Bonzanigo [A7], namely, the substitution of the

101

direct-method discrete Fourier transform (DFT) by the Goertzel algo-
rithm. Typical image spectra suffer from severe leakage and aliasing,
resulting in a downgraded performance of the algorithm, however. As a
remedy, we shall suggest some simple pre-processing techniques.

AII. THEORETICAL BACKGROUND

Let $\{x[n,m]\}$ be a finite image sequence and

$$X(u,v) = F\{x[n,m]\} = \sum_{n=0}^{N-1} \sum_{m=0}^{M-1} x[n,m] \exp(-j2\pi (\frac{nu}{N} + \frac{mv}{M})) \qquad (A1)$$

its discrete Fourier transform (DFT), briefly referred to as the
spectrum of $x[.]$. Without loss of generality, the image boundaries
are set $N = M$. Note that $X(u,v)$ is a continuous, generally complex
function and can be written as either

$$X(u,v) = X_R(u,v) + j X_I(u,v) \qquad (A2)$$

or as

$$X(u,v) = X_A(u,v) \exp \{j \arg [X(u,v)]\} , \qquad (A3)$$

with $X_R(.)$ the real part, $X_I(.)$ the imaginary part, $X_A(.)$ the amplitude
and $\arg[X(.)]$ the phase of the spectrum. The evaluation of amplitude
and phase as the magnitude

$$|X(u,v)| = (X_R^2(u,v) + X_I^2(u,v))^{\frac{1}{2}} \qquad (A4)$$

and the principle phase

$$ARG[X(u,v)] = \arctan \frac{X_I(u,v)}{X_R(u,v)} \qquad (A5)$$

leads to the following ambiguities: (i) the amplitude is forced to be
non-negative. Hence, whenever $X_A(.)$ crosses the complex plane from the
first to the third quadrant, passing through zero, or vice versa, the
phase experiences a discontinuity of $\pm \pi$. (ii) ARG $[X(.)]$, being the

principle phase, leads to "wrap-around" effects modulo 2π. Figure A1
visualizes these two conditions. A fictitious phasor, i.e., the locus
of the complex spectrum in the complex plane, experiences a phase dis-
continuity of $+\pi$ (case (i), Fig. A1a) and of -2π (case (ii), Fig. A1b).
Note that our definition of the arctangent function coincides with the
ATAN2(B,A) function in ANSI-FORTRAN, and not with ATAN(X). The dif-
ferences are illustrated in Table A1.
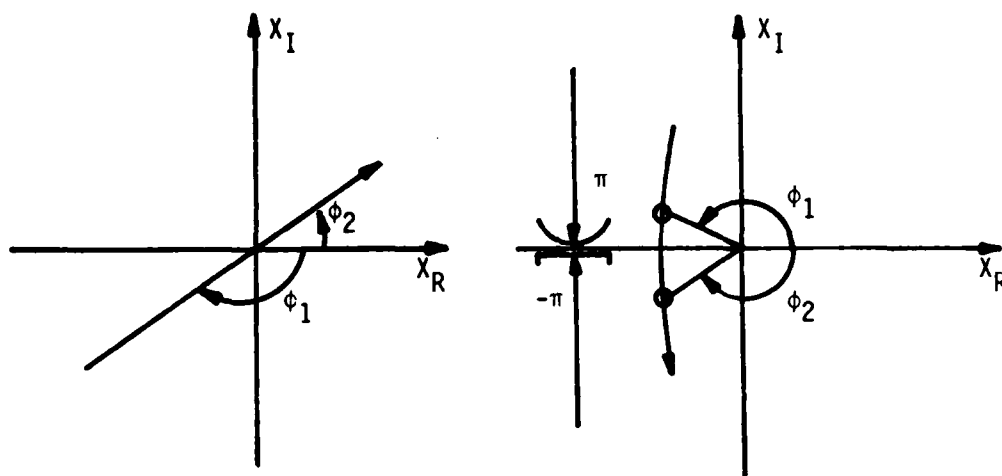

Figure A1. Discontinuities of the principle phase: a) case (i),
b) case (ii).

Table A1. ATAN2 and ATAN FORTRAN functions.

Phase (degr.)	ATAN2	ATAN
0	0	0
45	45	45
90	90	-90
135	135	-45
180	-180	0
225	-135	45
270	- 90	-90
315	- 45	-45
360	0	0
405	45	45

The derivatives of a two-dimensional spectrum can be obtained as [A8, p. 278].

$$\frac{dX(u,v)}{du} = F\{-jnx[n,m]\} = X'_{Ru}(u,v) + jX'_{Iu}(u,v) \tag{A6}$$

$$\frac{dX(u,v)}{dv} = F\{-jmx[n,m]\} = X'_{Rv}(u,v) + jX'_{Iv}(u,v) \tag{A7}$$

with the subscripts standing: R for real part, I for imaginary part, u for derivative with respect to u, v derivative with respect to v. It can be shown that, with the real and imaginary parts of (A6) and (A7), the derivative of the phase and amplitude are

$$\frac{d \ \arg[X(u,v)]}{du} = \frac{X_R X'_{Iu} + X'_{Ru} X_I}{X_R^2 + X_I^2} \tag{A8}$$

and

$$\frac{d \ A_X(u,v)}{du} = \frac{X_R X'_{Ru} + X_I X'_{Iu}}{(X_R^2 + X_I^2)^{\frac{1}{2}}} \tag{A9}$$

(and equivalently for the derivatives with respect to v).

With the total image "brightness" mass

$$X(0,0) = \sum_{n=0}^{N-1} \sum_{m=0}^{M-1} x[n,m] = X_R(0,0) \tag{A10}$$

and the derivative of the spectrum at the origin as

$$\frac{dX(0,0)}{du} = -j \sum_{n=0}^{N-1} \sum_{m=0}^{M-1} n \cdot x[n,m] = -jX'_I u(0,0), \tag{A11}$$

the derivative of the phase at u = 0, v = 0 is obtained as

$$\frac{d \ \arg \ [X(0,0)]}{du} = \frac{X'_{Iu}(0,0)}{X_R(0,0)} \tag{A12}$$

The right-hand side of (A12), however, is nothing but the negative value of the n-coordinate of the center of (brightness) gravity of the image. Equivalently, the center of gravity in m-direction is equal to the negative phase slope in v-direction.

AIII. TRIBOLET'S PHASE UNWRAPPING

Tribolet's unwrapping algorithm [A1] for the one-dimensional phase is based on the fast Fourier transform (FFT) of the data, and the FFT of the data premultiplied with the index, giving the complex conjugate derivative of the spectrum. With the initial phase value defined as zero, the principle value is compared with an unwrapped phase estimate obtained by a trapezoidal integration of the phase derivative. Whenever the difference is close to an integer multiple of π, say $k \cdot \pi$, then this value of $k \cdot \pi$ is added to the principle phase giving the unwrapped phase. However, if the difference is larger than a given threshold and/or if the difference of consecutive estimated phase values is much different from the average phase derivative, no decision is made and a subprogram called.

Within this subprogram, the values of the principle phase and the phase derivative are calculated in between the FFT frequencies, i.e., $\{\omega_k = (2\pi/N) \cdot k, k=0, 1, \ldots N-1\}$, N being the record length.

With subsequently increasing subdivisions of one interval of neighboring FFT frequencies, more and more values are calculated until the behavior of the phase is consistent with its estimate. Since for a phase which frequently changes its direction, the number of additionally needed DFT calculations can become very high, Bonzanigo [A7] suggested the use of the Goertzel algorithm [A2] (including a phase correction term) instead of the direct method, thus reducing the number of real multiplications by half.

AIV. IMPROVEMENT OF PERFORMANCE

Two effects are likely to limit the performance of Tribolet's algorithm: aliasing and leakage (also called Gibb's phenomenon). Aliasing results from under-sampling, leakage from the finite extension of the data record and any discontinuities within the data record [A8, p. 58].

Leakage can be explained as the convolution of a sinc-function, i.e., the spectrum of the record-limiting window, with the generalized spectrum of an infinite data record. Thus leakage becomes very severe for an abrupt termination of the signal.

Leakage leads to ripples in the spectrum in between the Fourier frequencies. To illustrate, consider the simple function in Fig. A2a, with Fig. A2b its principle phase and Fig. A2c the phase derivative evaluated at the FFT frequencies according to (A8). At first glance, the phase seems to be linear (in accordance with the phase one would expect from an infinite record), hence the phase derivative Fig. A2c should be constant. Figure A2d, however, shows the phase behavior in between FFT frequencies. The ripples appear and indicate why the phase derivative of the signal Fig. A2a, evaluated at the FFT frequencies, is not constant. Note that the leakage effect in this case arises mainly because of the overall non-zero signal component. In order to follow ripples and a generally steep phase, Tribolet's algorithm can perform satisfactorily only if the thresholds are set small. This again leads to numerous additional DFT calculations at intermediate frequencies, thus imposing CPU time problems.

Unfortunately it appears that leakage and aliasing are common problems in image processing. Note that image signals are usually
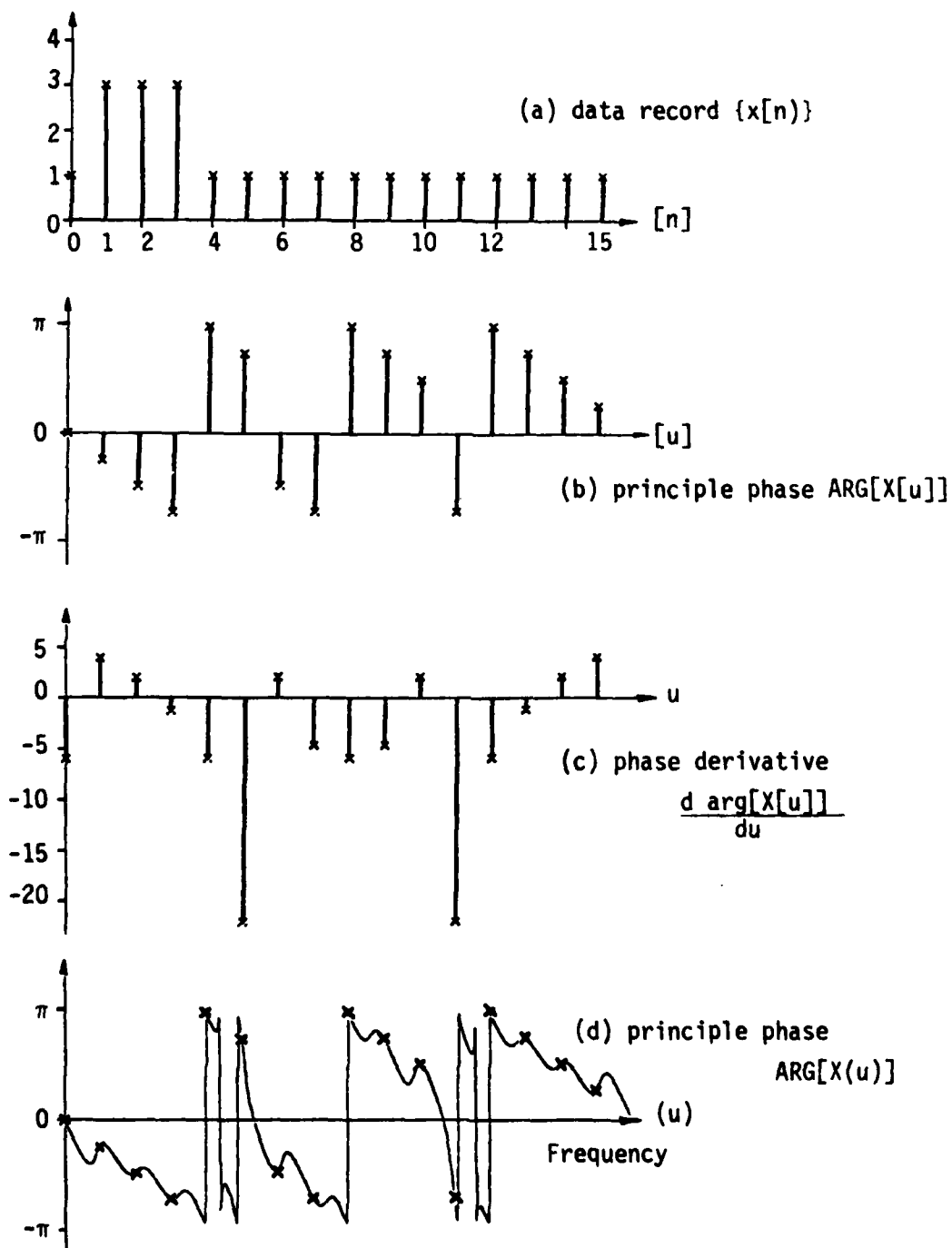
Figure A2. One-dimensional phase example.

non-negative and terminated abruptly at the boundaries. To some degree almost all digital images are under-sampled.

Leakage can be reduced by making the transition at the image boundary less "abrupt." This could be done by (i) subtracting the minimum pixel value from the total image, thus "lowering" the overall image surface, or (ii) data windowing. Furthermore, the phase slope average can be reduced, and thus the frequency of wrap-around occurrences reduced, by shifting the center of gravity into the data origin. This way, part of the data is shifted into the negative (non-causal) half plane. As an example, consider the signal given in Fig. A3(a). Figure A3(b) shows the principle phase and Fig. A3(c) the phase derivative at the FFT frequencies without pre-processing. Figure A3(d) was obtained by subtracting the minimum value of $x(n)$ from the whole record and shifting the origin into the center of travity. To obtain the FFT spectrum, the signal values about the negative axis can be attached to the right end (Fig. A3(e)), as if an identical period is following. Care has to be taken only with the pre-multiplication of the data in order to evaluate the phase derivative (Eq. (A6) and (A8)). The values attached to the right end are to be premultiplied with the negative indices according to Fig. A3(d). The same caution is necessary for the DFT evaluation at the intermediate frequencies. Whereas the FFT is identical to the Fourier series of a periodic extension of the data, the DFT at intermediate frequencies is not, but rather the spectrum of a zero padded version of Fig. A3(d). Hence the negative indices for a part of the signal have to be taken into account. Figure A3(f) now depicts the principle phase of Fig. A3(d) and Fig. A3(g) the phase derivative (at the FFT frequencies). The reduction in the number of
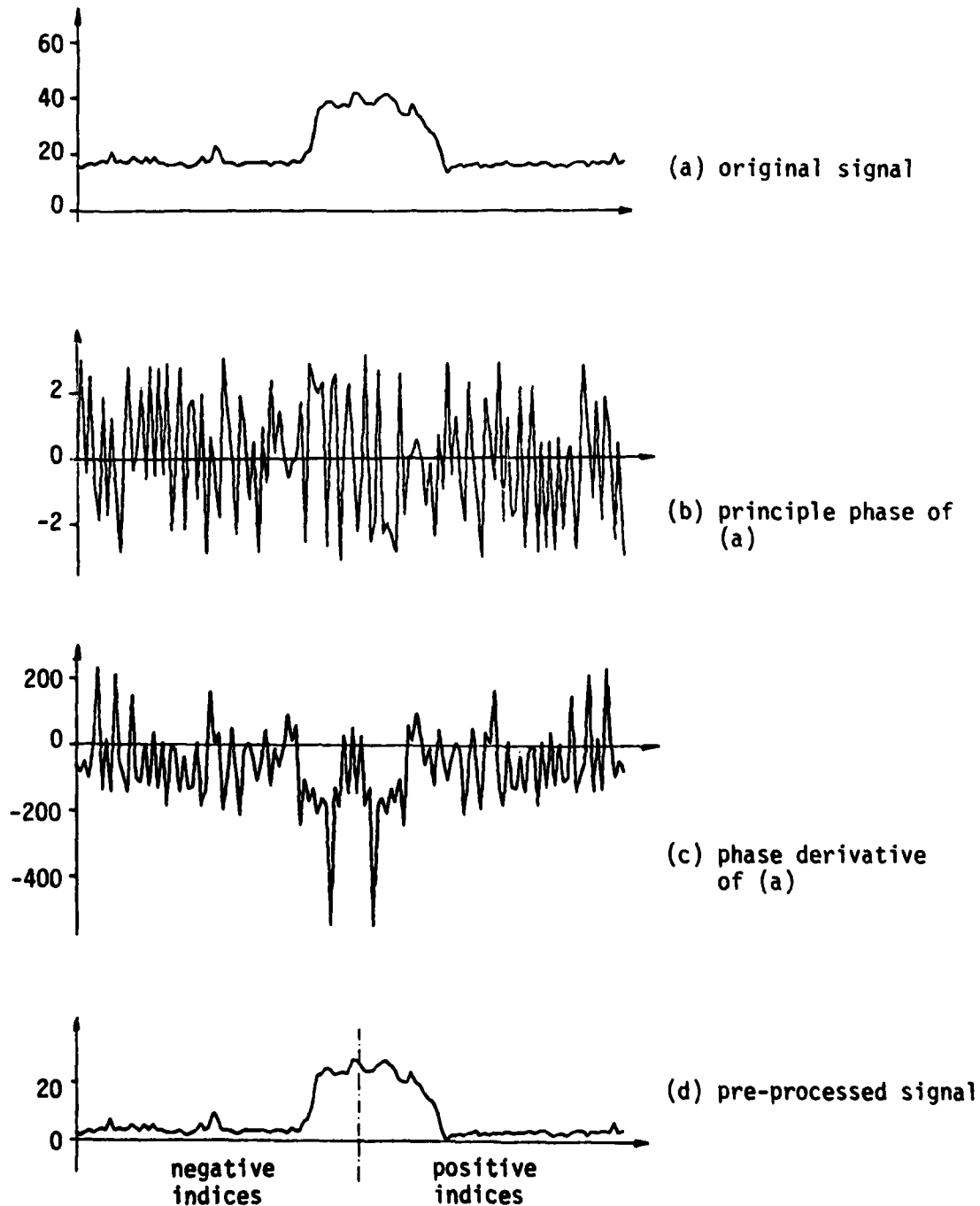
Figure A3. Phase unwrapping of a pre-processed signal.

(e) signal set-up for FFT

(f) principle phase of (e)

(g) phase derivative of (e)
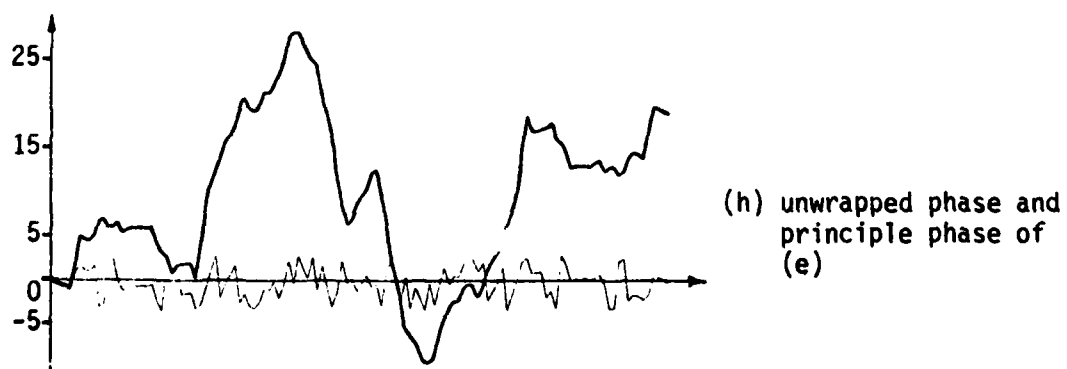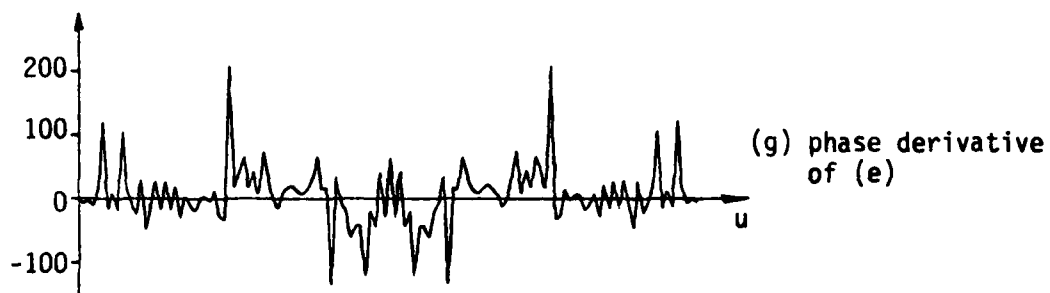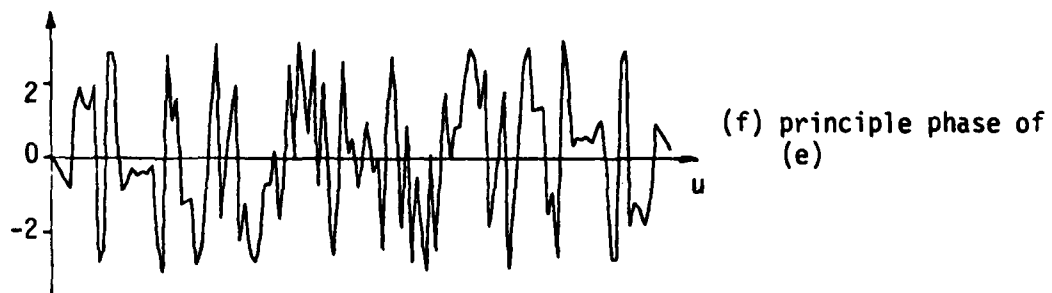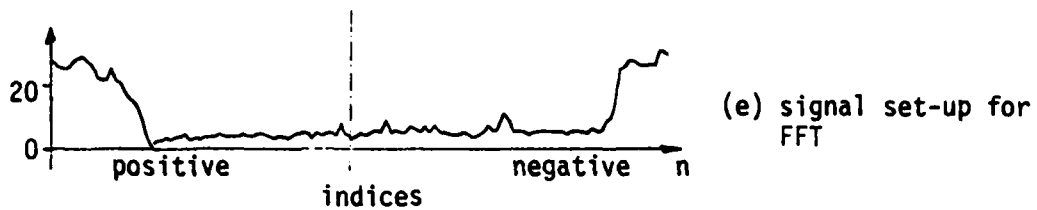
(h) unwrapped phase and principle phase of (e)

Figure A3 (cont.). Phase unwrapping of a pre-processed signal.

phase wrap-arounds becomes apparent, and with Tribolet's algorithm, including the modifications as described above, the unwrapped phase Fig. A3(h) was obtained. Since the displacement of the center of gravity into the origin has the effect of extracting a linear phase component, the resulting phase sequence is ready for the evaluation of the complex cepstrum.

AV. TWO-DIMENSIONAL PHASE UNWRAPPING

Consider an image sequence {x[n,m]} being shifted in the n,m-plane such that the origin n=0, m=0 has minimum distance to the center of gravity. With its region of definition $-K \leq n \leq L$, $-I \leq m \leq J$, the DFT becomes

$$X(u,v) = \sum_{n=-K}^{L} \sum_{m=-I}^{J} x[n,m] \exp(-j2\pi(\frac{nu}{N} + \frac{mv}{M})) \tag{A13}$$

Note that the DFT is defined for all real frequency numbers u and v. For the set of integer numbers within the u,v - plane, we introduce the notation [u], [v], and the spectrum at these points is

$$X[u,v] = \sum_{n=-K}^{L} \sum_{m=-I}^{J} x[n,m] \exp(-j2\pi(\frac{n[u]}{N} + \frac{m[v]}{M})) \tag{A14}$$

We shall refer to Eq. (A14) as the FFT-spectrum. Since
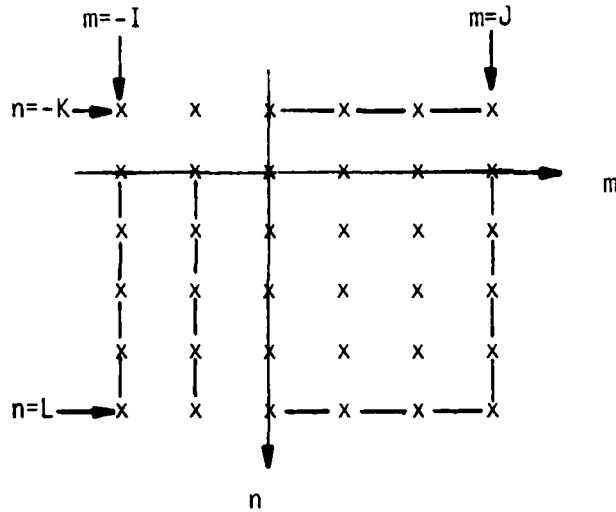
$$\exp(-j2\pi \frac{-k[u]}{N}) = \exp(-j2\pi \frac{(N-k)[u]}{N}) \tag{A15}$$

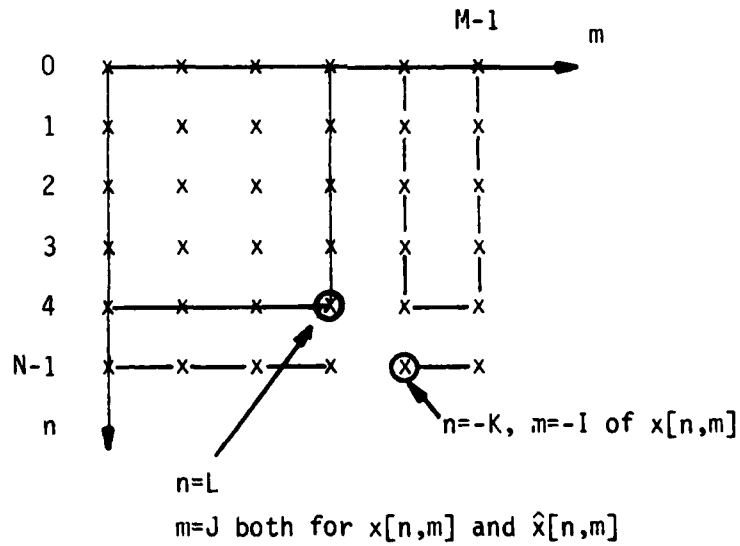the FFT spectrum (not the DFT) can be written for positive summation indices as

$$X[u,v] = \sum_{n=0}^{N-1} \sum_{m=0}^{M-1} \hat{x}[n,m] \exp(-j2\pi(\frac{n[u]}{N} + \frac{m[v]}{M})) \tag{A16}$$

with $\hat{x}[n,m]$ the periodic extension of $x[n,m]$ (see Fig. A4a and A4b).
A mixed "DFT/FFT" is defined for those frequency numbers with only one
coordinate being integer, i.e.,

(a) image $x[n,m]$

n=L

m=J both for $x[n,m]$ and $\hat{x}[n,m]$

(b) image $\hat{x}[n,m]$

Figure A4. Original image and periodic extension.

$$X(u,[v]) = \sum_{n=-K}^{L} \sum_{m=-I}^{J} x[n,m] \exp(-j2\pi(\frac{nu}{N} + \frac{m[v]}{M}))$$

$$= \sum_{n=-K}^{L} \exp(-j2\pi\frac{nu}{N}) \sum_{m=0}^{M-1} x_m[n,m] \exp(-j2\pi\frac{m[v]}{M}) \qquad (A17)$$

The sequence $x_m[n,m]$ is a periodic extension of $x[n,m]$ only in m-direction. Similarly,

$$X([u],v) = \sum_{m=-I}^{J} \exp(-j2\pi\frac{mv}{M}) \sum_{n=0}^{N-1} x_n[n,m] \exp(-j2\pi\frac{n[u]}{N}) \qquad (A18)$$

with $x_n[n,m]$ the periodic extension in n-direction.

It is not necessary to generate three different periodic extensions. Even the mixed DFT/FFT can be performed on the data $\hat{x}[n,m]$ by re-arrangement of the summation terms. This is explained here only for the spectrum $X(u, [v])$:

Define the vectors

$$\hat{Y}(n;[v]) = \sum_{m=0}^{M-1} \hat{x}[n,m] \exp(-j2\pi\frac{m[v]}{M}) \qquad (A19)$$

and

$$Y_m(n;[v]) = \sum_{m=0}^{M-1} x_m[n,m] \exp(-j2\pi\frac{m[v]}{M}) \qquad (A20)$$

Then

$$Y_m(n;[v]) = \begin{cases} \hat{Y}(n;[v]) & \text{for } 0 \le n \le L \\ \hat{Y}(L-n;[v]) & \text{for } -K \le n \le -1. \end{cases} \qquad (A21)$$

Hence the row-FFT $\hat{Y}(n;[v])$ is performed on the set $\hat{x}[n,m]$, and, for a column-FFT, the output does not have to be re-ordered. For a column-DFT, however, the summation terms have to be re-arranged according to Eq. (A21).

The two-dimensional phase unwrapping technique proposed in this work is designed as follows. Only one vector (i.e., row or column) in the frequency domain is unwrapped at a time. To obtain the initial unwrapped phase values, the phase is unwrapped for the first column ($[u] = 0$) or row ($[v] = 0$). With these values, the phase is unwrapped row by row (or column by column) along integer frequency numbers. Thus, whenever the DFT is to be calculated at intermediate frequencies, a mixed mode DFT/FFT can be applied.

To obtain the phase derivatives, the spectrum of $n \cdot x[n,m]$ and $m \cdot x[n,m]$ is needed. Note that n,m are defined as $-K \leq n \leq L$ and $-I \leq m \leq J$. Hence, to obtain the FFT, the image is to be extended periodically, but the negative pre-multiplication has to be preserved. The mixed DFT/FFT of $n \cdot x[n,m]$ then is given as:

$$Z_n(u,[v]) = \sum_{n=-K}^{L} \sum_{m=-I}^{J} n \cdot x[n,m] \, \exp(-j2\pi(\frac{nu}{N} + \frac{mv}{M}))$$

$$= \sum_{n=-K}^{L} n \cdot \exp(-j2\pi\frac{nu}{N}) \sum_{m=-I}^{J} x[n,m] \, \exp(-j2\pi(\frac{m[v]}{M}))$$

$$= \sum_{n=-K}^{L} n \cdot \exp(-j2\pi\frac{nu}{N}) \cdot Y_m(n;[v]). \tag{A22}$$

Hence, pre-multiplication is not a part of the row FFT, but of the column DFT. A similar expression can be obtained for

$$Z_m([u],v) = \sum_{n=-K}^{L} \sum_{m=-I}^{J} m \cdot x[n,m] \, \exp(-j2\pi(\frac{nu}{N} + \frac{mv}{M})). \tag{A23}$$

Since the derivative is needed only with respect to the direction of unwrapping along an integer valued frequency coordinate, the evaluation of $Z_n([u],v)$ and $Z_m(u,[v])$ is not needed.

The following list is a summary of all steps introduced above (see Fig. A5). It was chosen to unwrap the phase row-wise, with the initial values obtained from unwrapping the first column.

A) Shift center of origin of n,m-plane to center of gravity and obtain $\hat{x}[n,m]$ by periodic extension according to Fig. A4.

B) Unwrap first column arg $X[u,1]$

   1) do row-FFT on $\hat{x}[n,m]$ giving $\hat{Y}([n];[v])$ vectors. Actually, since only $\hat{Y}([n];[0])$ is of interest, the FFT reduces to the simple summation

   $$\hat{Y}([n];[0]) = \sum_{m=0}^{M-1} \hat{x}[n,m]. \tag{A24}$$

   2) To obtain the principle phase, phase derivative etc., perform the (column) FFT on $\hat{Y}([n];[0])$, giving $X([u],[0])$, and also on $n \cdot \hat{Y}([n];[0])$, with the factor n according to the re-ordered scheme, giving $Z_n([u],[0])$.

   3) If the (column) DFT is needed, i.e., $X(u,[0])$ and $Z_n(u,[0])$, a re-ordered summation of $\hat{Y}([n],[0])$, and $n \cdot Y([n];[0])$ is required.

C) Unwrap all phase rows arg $X[u,v]$

   1) column FFT's on $\hat{x}[n,m]$

   2) do row by row [u]

      --look up starting value

      --FFT $\rightarrow X[u,v]$

      --pre-multiply correctly, and FFT $\rightarrow Z_m[u,v]$

      --if DFT is needed: re-order m-summation, and DFT's give $X([u],v)$ and $Z_m([u],v)$.
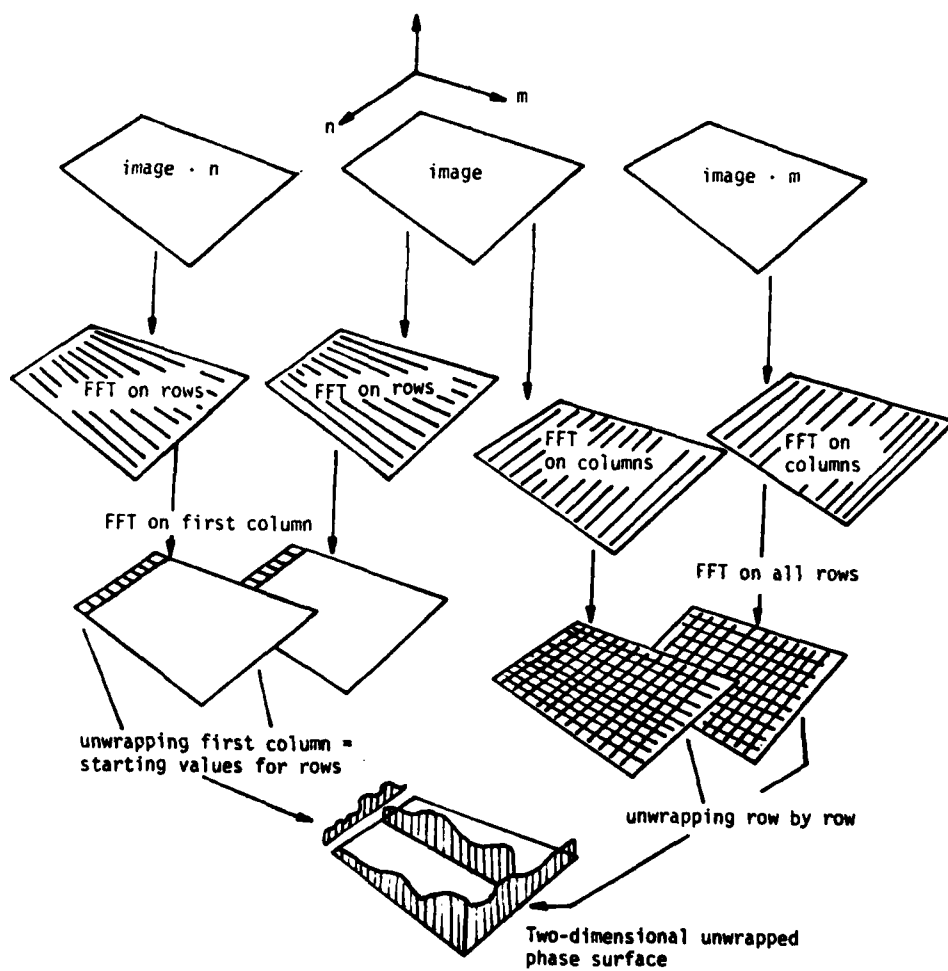
116

Figure A5. Unwrapping a two-dimensional phase surface.

Since unwrapping is performed vector-wise, Tribolet's algorithm can be utilized with the following minor changes:

--the input data is complex

--pre-multiplication and DFT summation terms need occasional re-ordering of indices.

AVI.   RESULTS

By shifting the image origin to the nearest pixel location of the center of luminance gravity, phase plots were obtained with a derivative of almost zero at the spectral origin.

During the generation of various phase surfaces, however, it was discovered that the smoothness of the surface plot could be drastically improved, and thus the number of DFT calculations minimized, by choosing a different point of the image as the spatial origin.

This point is to be selected such that the unwrapped phase at the end points of the frequency range are close to zero. With the signal and spectrum related to each other by Eq. (A1), a shift of the image by n_0, m_0 is equivalent to a linear phase shift, according to

$$x(n-n_0,m-m_0) = X(u,v) \exp(-j2\pi(\frac{n_0 u}{N} + \frac{m_0 v}{M})).$$ (A25)

The required phase shift then is determined by evaluating the unwrapped phase arg $[X(0,M)]$ and arg$[X(N,0)]$. Since these values are calculated by essentially one-dimensional unwrapping procedures, they are obtained fast.

In addition to this improvement it was desired to obtain a phase surface with its spectral origin at the center. This was achieved by exploiting the conjugate symmetry of the spectrum.

Figure A6 serves as an example for such an unwrapped phase surface. Note that the unwrapped phase is very sensitive to estimation errors in spectral regions of low energy, i.e., where the phasor is close to its origin [A9].
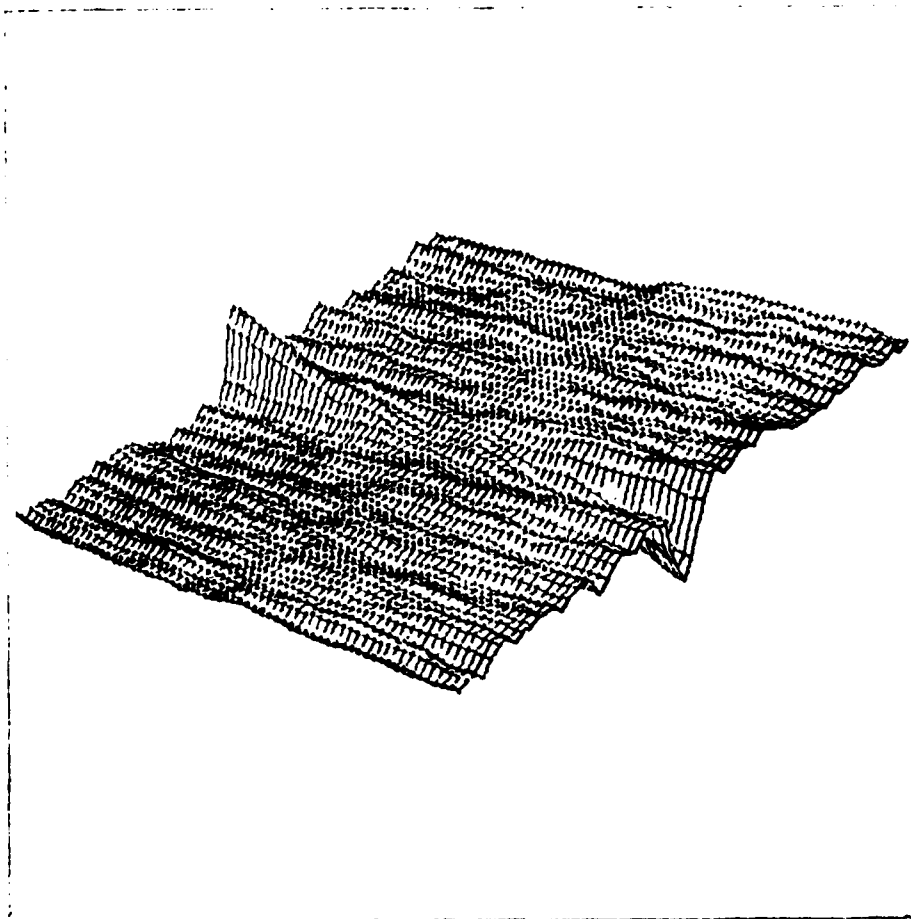

Figure A6.   Example of unwrapped two-dimensional phase.

APPENDIX REFERENCES

[A1] J.M. Tribolet, "A new phase unwrapping algorithm," IEEE Trans. Acoust., Speech, Signal Processing, vol. ASSP-25, pp. 170-177, Apr. 1977.

[A2] A.V. Oppenheim, J.S. Lim, G. Kopec and S.C. Pohlig, "Phase in speech and pictures," in: Proc. IEEE Int. Conf. Acoust., Speech, Signal Processing, Washington, D.C., April 1979.

[A3] T.S. Huang, J.W. Burnett, and A.G. Deczky, "The importance of phase in image processing filters," IEEE Trans. Acoust., Speech, Signal Processing, vol. ASSP-23, pp. 529-542, Dec. 1975.

[A4] S.C. Pohlig, "Fourier transform phase coding of images," IEEE Trans. Acoust., Speech, Signal Processing, vol. ASSP-28, pp. 339-341, June 1980.

[A5] A.V. Oppenheim and R.W. Schafer, "Digital Signal Processing," Englewood Cliffs, N.J.: Prentice-Hall, 1975.

[A6] D.E. Dudgeon, "The existence of cepstra for two-dimensional rational polynomials," IEEE Trans. Acoust., Speech, Signal Processing, vol. ASSP-23, pp. 242-243, Apr. 1975.

[A7] F. Bonzanigo, "An improvement of Tribolet's phase unwrapping algorithm," IEEE Trans. Acoust., Speech, Signal Processing, vol. ASSP-26, pp. 104-105, Fib. 1978.

[A8] A. Papoulis, "Signal Analysis," New York: McGraw-Hill, 1977.

[A9] T.F. Quatieri, Jr., "Minimum and Mixed Phase Speech Analysis--Synthesis by Adaptive Homomorphic Deconvolution," IEEE Trans. Acoust., Speech, Signal Processing, vol. ASSP-27, pp. 328-335, Aug. 1979.

ATE
LMED
-8